



HAL
open science

Influence of the Gulf of Guinea islands on the Atlantic Equatorial Undercurrent circulation

D. Napolitano, Gael Alory, I. Dadou, Y. Morel, J. Jouanno, G. Morvan

► **To cite this version:**

D. Napolitano, Gael Alory, I. Dadou, Y. Morel, J. Jouanno, et al.. Influence of the Gulf of Guinea islands on the Atlantic Equatorial Undercurrent circulation. *Journal of Geophysical Research. Oceans*, In press, 10.1029/2021JC017999 . hal-03780249v2

HAL Id: hal-03780249

<https://hal.science/hal-03780249v2>

Submitted on 19 Sep 2022

HAL is a multi-disciplinary open access archive for the deposit and dissemination of scientific research documents, whether they are published or not. The documents may come from teaching and research institutions in France or abroad, or from public or private research centers.

L'archive ouverte pluridisciplinaire **HAL**, est destinée au dépôt et à la diffusion de documents scientifiques de niveau recherche, publiés ou non, émanant des établissements d'enseignement et de recherche français ou étrangers, des laboratoires publics ou privés.

Influence of the Gulf of Guinea islands on the Atlantic Equatorial Undercurrent circulation

D. C. Napolitano¹, G. Alory¹, I. Dadou¹, Y. Morel¹, J. Jouanno¹, and G. Morvan¹

¹Laboratoire d'Etudes en Géophysique et Océanographie Spatiales (LEGOS), Université de Toulouse, CNES, CNRS, IRD, UT3. Toulouse, France

Key Points:

- Velocity observations show that the EUC hits São Tomé Island at 6°E, forcing the jet to bifurcate earlier than if the island did not exist;
- The EUC dynamics and the location of São Tomé impose an asymmetry to the bifurcation, affecting net zonal fluxes in the tropical Atlantic;
- The EUC-island encounter triggers vertical advection and transformation of the EUC water via diapycnal and isopycnal mixing and friction.

Corresponding author: Dante C. Napolitano, dante.napolitano@univ-brest.fr
current affiliations: Univ. Brest, CNRS, Ifremer, IRD, Laboratoire d'Océanographie Physique et Spatiale (LOPS), IUEM, F29280, Plouzané, FR.

This article has been accepted for publication and undergone full peer review but has not been through the copyediting, typesetting, pagination and proofreading process, which may lead to differences between this version and the [Version of Record](#). Please cite this article as [doi: 10.1029/2021JC017999](https://doi.org/10.1029/2021JC017999).

This article is protected by copyright. All rights reserved.

Abstract

In the easternmost portion of the Gulf of Guinea, Bioko Island marks the beginning of an island chain that stretches NE–SW to the Equator, where São Tomé Island sits in the path of the Equatorial Undercurrent (EUC). In this study, we explore the meso-to-large-scale effects of local flow-topography interactions that escalate from the EUC encounter with the Gulf of Guinea islands. A mean shipboard ADCP section captures the EUC as a strong subsurface jet that ultimately hits São Tomé. Motivated by these observations, we ran two ocean general circulation model simulations that differ by the presence versus absence of the Gulf of Guinea islands. Diagnostics of salinity and potential vorticity (PV) from these simulations show that the EUC bifurcates at 6°E, triggering mesoscale activity that spreads the EUC waters. On both sides of São Tomé, the EUC branches roll up into eddies that propagate westward. These low-PV anticyclones carry high salinity through the tropical Atlantic, introducing PV anomalies along eddy corridors mirrored by the Equator. The formation of such eddies is affected by diapycnal and isopycnal mixing and friction, and their distribution between hemispheres is intrinsically related to the location of São Tomé. The eddies are modulated at both seasonal and interannual scales. A strong EUC generates numerous and stronger eddies, while seasonal equatorial upwelling indirectly hinders their formation. Convergence of the EUC upstream of São Tomé reveals intense downwelling and freshening, whereas divergence and upwelling are associated with the EUC negotiating the island.

Plain Language Summary

In the eastern portion of the tropical Atlantic, in the Gulf of Guinea, Bioko Island marks the beginning of an island chain that stretches NE–SW to the Equator, where São Tomé Island sits in the path of the strongest current in the tropical Atlantic, the Equatorial Undercurrent (EUC). The EUC connects the tropical Atlantic, transporting high-salinity waters eastward. In this study we explore the effects of flow-topography interactions on the EUC circulation. Velocity observations capture the EUC as a strong current that hits São Tomé Island. Motivated by these observations, we ran two model simulations that differ by the presence versus absence of the Gulf of Guinea islands. Diagnostics of salinity and potential vorticity (a dynamical quantity that relates to the circulation) show that the EUC bifurcates at 6°E, spreading the EUC waters. On both sides of São Tomé Island, the EUC branches form eddies that propagate westward through the tropical Atlantic. The formation and distribution of such eddies present an asymmetry between hemispheres due to the EUC interaction with São Tomé. On regional scales, a particle-tracking experiment reveals sinking before the particles reach São Tomé, with mixing and freshening of the EUC waters as they flow around the island.

1 Introduction

The Equatorial Undercurrent (henceforth EUC) is the strongest zonal current in the tropical Atlantic, dominating its large-scale circulation and intrabasin exchange. This current originates from one of the multiple North Brazil Current retroreflections (e.g., Schott et al., 1998; Silveira et al., 2000; Goes et al., 2005), and contributes to the cross-equatorial salt and heat transport and subtropical-cell circulation which impacts the Atlantic Meridional Overturning Circulation (AMOC; e.g., Hazeleger et al., 2003; Rabe et al., 2008; Chang et al., 2008), transporting eastward mainly the saline and oxygen-rich Salinity Maximum Water (SMW; $T > 24^{\circ}\text{C}$, $S > 37$) and South Atlantic Central Water (SACW; $T > 13^{\circ}\text{C}$, $S > 35$) subducted in the subtropics (e.g., Stramma & Schott, 1999; Mémerly et al., 2000; Blanke et al., 2002; Snowden & Molinari, 2003) to surface in the central and eastern equatorial Atlantic (e.g., Jouanno, Marin, Du Penhoat, Molines, & Sheinbaum, 2011; Jouanno, Marin, Du Penhoat, Sheinbaum, & Molines, 2011). Taken as the Atlantic counterpart of the previously studied Pacific Equatorial Undercurrent, the structure of

64 the Atlantic EUC was described by Metcalf et al. (1962) from sections of temperature,
65 salinity, oxygen, and direct measurements of velocity and current shear. More recent stud-
66 ies improved the observational spatio-temporal resolution in the region, with Conductivity-
67 Temperature-Depth (CTD), Acoustic Doppler Current Profiler (ADCP), and current moor-
68 ing observations (e.g., Brandt et al., 2006; Kolodziejczyk et al., 2009; Johns et al., 2014)
69 to understand the EUC structure and variability. In the present paper, we use a numer-
70 ical model with improved bathymetry resolution to focus on a question which has not
71 received particular attention: the impact of the Gulf of Guinea islands on the circula-
72 tion of the EUC.

73 The EUC flows eastward at $> 0.4 \text{ ms}^{-1}$ along the Equator, with reports of $> 0.7 \text{ ms}^{-1}$
74 close to the center of the basin (23°W ; Brandt et al., 2006). The current transport pro-
75 gressively decreases eastward, from $\sim 14 \text{ Sv}$ at 23°W (Brandt et al., 2014; Johns et al.,
76 2014) to $\sim 12 \text{ Sv}$ at 10°W (Kolodziejczyk et al., 2009; Johns et al., 2014), $\sim 10.5 \text{ Sv}$ at 0°
77 (Johns et al., 2014; Kolodziejczyk et al., 2014), and $\sim 4 \text{ Sv}$ at 6°E (Kolodziejczyk et al.,
78 2014). These transports present variability at intraseasonal (Brandt et al., 2006; Jouanno
79 et al., 2013), semiannual (Brandt et al., 2006; Johns et al., 2014), and interannual (Brandt
80 et al., 2021) time scales, captured by both modeling and observational efforts, which con-
81 tinue to improve under the umbrella of projects such as PIRATA (Prediction Research
82 Moored Array in the Tropical Atlantic; Bourlès et al., 2008, 2019), AtlantOS (Optimis-
83 ing and Enhancing the Integrated Atlantic Ocean Observing Systems; [https://www.atlantos-
84 h2020.eu/](https://www.atlantos-h2020.eu/)), TAOS (The Tropical Atlantic Observing System; Foltz et al., 2019), and
85 TRIATLAS (Tropical and South Atlantic Climate-Based Marine Ecosystem Prediction
86 for Sustainable Management; <https://triatlas.w.uib.no/>) among others.

87 In the eastern Gulf of Guinea, the EUC approaches the region near 6°E , where the
88 maximum salinity associated with the EUC bifurcates and westward return flows appear
89 north and south of the Equator (e.g., Kolodziejczyk et al., 2014). Although the source
90 waters and the retroreflections at the origin of the EUC have been extensively studied (e.g.,
91 Schott et al., 1998; Stramma & Schott, 1999; Mémery et al., 2000; Silveira et al., 2000;
92 Snowden & Molinari, 2003; Blanke et al., 2002; Goes et al., 2005, and others), little is
93 known about its bifurcation on the eastern basin and the formation of the returning west-
94 ward flows (e.g., Gouriou & Reverdin, 1992; Kolodziejczyk et al., 2014; Assene et al., 2020).
95 Using observations and a $1/12^\circ$ numerical simulation, Kolodziejczyk et al. (2014) described
96 the seasonal cycle and bifurcation of the EUC between 5°E and the African continent,
97 a region termed “termination site” by the authors. They showed a robust EUC seasonal
98 cycle, with characteristic high-salinity waters present in the westward recirculations op-
99 posing the EUC in late boreal spring. Toward the end of summer, the EUC weakened
100 and saline waters were not observed within the inner portions of the gulf. More recently,
101 Assene et al. (2020) noted that the extra-equatorial westward return flows opposing the
102 EUC were in fact associated with the mesoscale dynamics of the EUC. Using a $2\frac{1}{2}$ -layer
103 model, McCreary and Yu (1992) showed that a EUC-like jet is inherently unstable and
104 shed anticyclonic eddies in both hemispheres. According to Assene et al. (2020), these
105 successive mesoscale eddies that propagate westward spread their potential vorticity (PV)
106 content to create zonal bands of nearly homogeneous PV. The eddies originate through
107 the inverse energy cascade by the merging of small-scale PV anomalies, which were tracked
108 back to the easternmost portions of the Gulf of Guinea (Assene et al., 2020) in a region
109 populated by islands.

110 Flow-island interactions are known to generate mesoscale eddies in different regions
111 of the ocean (e.g., Arístegui et al., 1994; Sangrà et al., 2009; Tchamabi et al., 2017). In
112 the eastern Gulf of Guinea, several islands align to form a NE–SW oriented island chain.
113 The three main islands, from the coastal to the open ocean—Bioko (3.5°N , 8.7°E), Príncipe
114 (1.6°N , 7.4°E), and São Tomé (0.2°N , 6.6°E)—stand in the path of ocean currents, with
115 flow-island interactions likely to affect the regional and larger-scale circulation. The south-
116 ernmost of the three islands, São Tomé, is equivalent to the renowned Galápagos Islands

117 (0.5°S, 91°W) in the Pacific, which have been shown to strongly interact with the Pa-
118 cific EUC. Karnauskas et al. (2007) showed that the obstruction of the Pacific EUC by
119 the Galápagos can significantly alter the circulation. Its bifurcation leads to main branches
120 that continue flowing eastward and join the continental slope, preferentially to the south
121 (e.g., Karnauskas et al., 2007; Montes et al., 2010), and to a partial return of the flow
122 westward (e.g., Johnson et al., 2002; Karnauskas et al., 2007). Comparing simulations
123 with and without the Galápagos islands at different resolution, Karnauskas et al. (2007)
124 showed that flow-island interactions lead to a deeper thermocline, which yield positive
125 SST anomalies and reduce the westward bias of the Pacific cold tongue, increasing sea
126 surface temperature and ocean-atmosphere fluxes. Such effects even influence the peri-
127 odicity of the El Niño Southern Oscillation (Karnauskas et al., 2008). Finally, the au-
128 thors stated that major changes are produced when the islands are implemented at suf-
129 ficient resolution on the model grid, otherwise even a strong flow such as the EUC would
130 only “glance” the islands (Karnauskas et al., 2007). This seems to be particularly the
131 case for Kolodziejczyk et al. (2014)’s simulation, which, despite having sufficient hori-
132 zontal resolution, fails to adequately resolve the islands in the Gulf of Guinea. In Kolodziejczyk
133 et al. (2014), one cannot clearly see these islands, and the EUC bypasses them to bifur-
134 cate at the African continent.

135 In a theoretical study, Pedlosky and Spall (2015) used a shallow water model to
136 represent the Pacific EUC interaction with Galápagos. For a “supercritical flow” as the
137 EUC, the current is affected locally by the island, with no standing Rossby wave field.
138 Their numerical solutions showed the formation of dipole-like PV anomalies on the lee
139 of the islands, which were also affected by placing the island asymmetrically from the
140 Equator (for this case, the authors displayed only the subcritical flow). With a proper
141 representation of islands, the *mise en scène* in the Gulf of Guinea suggests that simi-
142 lar consequences could arise from the interaction between islands and currents, particu-
143 larly due to the obstruction of the EUC’s strong zonal jet by São Tomé Island. In Kolodziejczyk’s
144 et al. (2014) configuration, the dynamics associated with the islands were not well cap-
145 tured. Later, Assene et al. (2020) suggested that mixing and frictional processes acting
146 near the islands could play a role in the dynamics of the EUC and return flows.

147 Downscaling from the mean tropical Atlantic circulation into the eastern Gulf of
148 Guinea, the primary objective of this study is to assess the impact of the Gulf of Guinea
149 islands on the meso-to-large-scale circulation of the EUC. We confirm from regional ob-
150 servations that the EUC hits São Tomé, and then discuss the repercussions of this in-
151 teraction using a numerical simulation focusing on how flow patterns and tracer trans-
152 port are affected by the EUC interaction with the islands. Throughout the paper, we
153 ask: (i) do the islands impact the bifurcation of the EUC?; (ii) can this interaction have
154 consequences for the return flows and the net fluxes across the Tropical Atlantic, espe-
155 cially through mesoscale dynamics?; and (iii) how do regional processes near the islands
156 impact the EUC dynamics?

157 2 Observational motivation and the numerical approach

158 2.1 Tropical Atlantic observations

159 To address the Gulf of Guinea islands’ topography effects on the EUC circulation,
160 we first identified the EUC along the Equator and west of São Tomé Island, from zonal
161 velocity (u) and salinity observations. We used shipboard ADCP sections (Bourlès et
162 al., 2018) at 6°E from five cruises—PIRATA Fr22, and EGEE 1, 2, 3, and 5 (processing
163 details in Herbert et al., 2015, individual cruises in supplementary information S1)—and
164 salinity measurements derived from a moored CTD at (0°N, 0°E) between 2007 and 2017,
165 part of the PIRATA buoy array (no velocity data is available for this particular buoy).
166 From each cruise track, we selected all ADCP velocity measurements between 2°S and
167 2°N, in a 0.1° box around 6°E. Continuous direct velocity measurements at the EUC

168 are scarce in the region, and we acknowledge that the five cruises may not provide season-
169 independent measurements for an ideal mean scenario (three cruises occur between May-
170 July, one in April, and one in September). Nevertheless, the cruises capture the variabil-
171 ity of the EUC in terms of strength, core depth, and latitudinal migration, showing par-
172 ticularly a stronger flow in EGEE2, EGEE5, and Fr22 and a weaker EUC in EGEE1 and
173 EGEE3. We created a mean state of the zonal component of the EUC by merging the
174 short time average (2 min) zonal velocity u from the cruises via objective mapping, with
175 correlation lengths three times the processed data sampling interval, $\Delta x = 0.20^\circ$ and
176 $\Delta z = 15$ m in the horizontal and vertical directions, respectively, which are sufficient
177 to resolve the EUC mesoscale dynamics of about 1° in the region. For the salinity, we
178 used the moored CTD data available within the Enhanced PIRATA dataset, a product
179 with additional quality control, no temporal gaps, and vertically mapped to a 5-m grid
180 (cf. Foltz et al., 2018).

181 Briefly, the analyzed datasets capture the EUC as a strong subsurface-intensified
182 jet flowing eastward at the Equator at 6°E , hammering São Tomé Island about 50 km
183 downstream (Fig. 1a). Motivated by these EUC observations, we ran two numerical sim-
184 ulations of the NEMO model (Nucleus for European Modelling of the Ocean; Madec
185 & the NEMO team, 2016), one reference simulation—hereafter NEMO With Islands (WI)—
186 and another without the topography of the islands of the Gulf of Guinea, the NEMO
187 No Islands (NI).

188 2.2 NEMO simulations

189 The reference simulation is an eddy-resolving configuration of the equatorial and
190 tropical Atlantic (20°S – 20°N , 60°W – 15°E) with $1/12^\circ$ horizontal resolution and 75 ver-
191 tical levels, nested in a $1/4^\circ$ resolution eddy-permitting parent grid. The two domains
192 are coupled online via the AGRIF library in two-way mode (Blayo & Debreu, 1999). We
193 enforced boundary conditions at the parent grid open boundaries using the MERCA-
194 TOR global daily reanalysis GLORYS2V4 (Ferry et al., 2012). At the surface, the fluxes
195 of momentum, heat, and freshwater are obtained from hourly outputs of the ERA5 re-
196 analysis (Copernicus Climate Change Service, 2017) using bulk formulae from Large and
197 Yeager (2009). There is no tidal forcing. Vertical mixing is parameterized using a tur-
198 bulent kinetic energy closure scheme (Blanke & Delecluse, 1993) and bottom friction is
199 quadratic. Both simulations were initialized with temperature and salinity from GLO-
200 RYS2V4 on 1 Jan 2005 and run for 2 years for model adjustment. We used daily-mean
201 outputs from the last 10 years of simulation (2007 to 2016). These configurations resolve
202 the equatorial and near-equatorial current systems and their embedded mesoscale vari-
203 ability. In our simulation, we interpolated the ETOPO2 bathymetry (ETOPO2, 2001)
204 directly into the $1/12^\circ$ grid. For the NI configuration, we removed grid points with depths
205 shallower than 1000 m and then linearly interpolated the gaps in the bathymetry prior
206 to running the simulation with the same initial conditions as WI. In practice, this means
207 that this experiment has no islands in the eastern Gulf of Guinea (4°S – 6°N , 0° – 12°E).
208 However, NI is not fully independent from the islands’ influence, since the wind forcing
209 is the same and potential effects of the islands on the wind stress curl would be present
210 in both simulations.

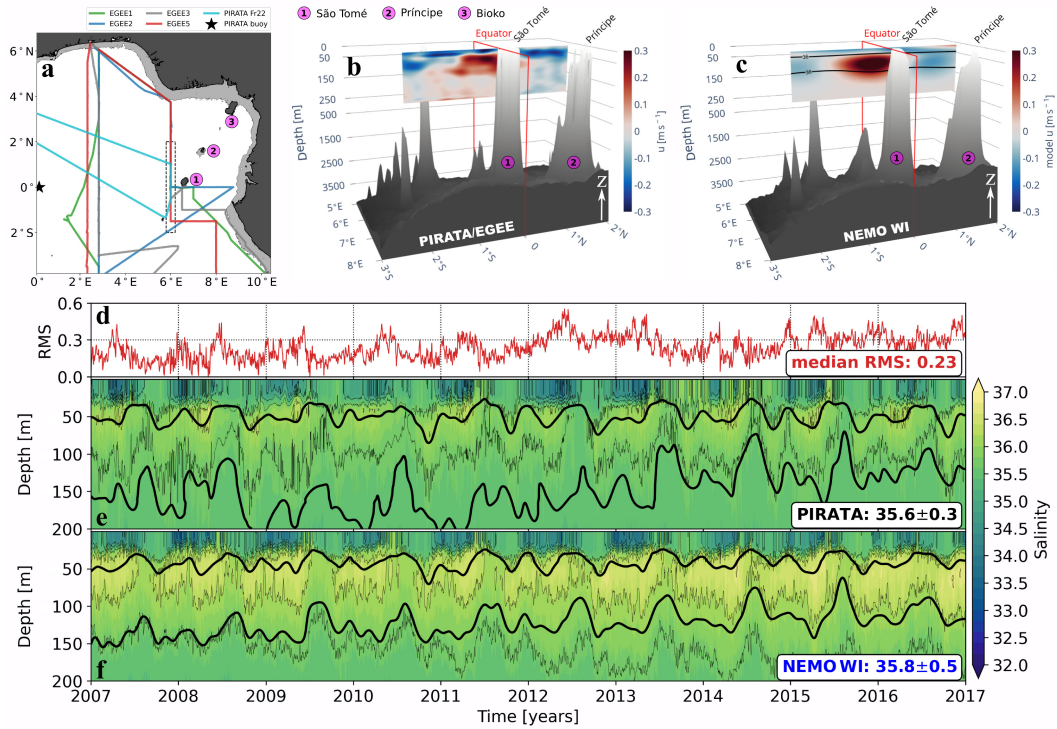


Figure 1. Comparison between observations and the NEMO reference (WI) numerical simulation. a) Map of the study region showing the location of the Gulf of Guinea islands (circles labelled 1 to 3), the five cruise tracks—PIRATA Fr22 (Apr 2012), EGEE 1 (Jun 2005), 2 (Sep 2005), 3 (Jun 2006), and 5 (Jun 2007)—and the moored buoy location (\star). The dashed box shows the area sampled for the ADCP vertical sections. b) Objectively mapped mean zonal velocity (positive eastward) from shipboard ADCP data at 6°E . The vertical axis is rescaled for the upper 500 m. c) NEMO 10-year-averaged vertical section of zonal velocity at 6°E ; black lines represent the 36 salinity contour. d) RMS difference series between daily vertical profiles of salinity at $(0^{\circ}\text{N}, 0^{\circ}\text{E})$, comparing (e) the enhanced PIRATA dataset buoy measurements with (f) the model series interpolated into the buoy vertical levels at the same location. In (e) and (f), thick black lines represent the 30-day filtered $1025.3\text{--}1026.4\text{ kg m}^{-3}$ density contours. The values in the horizontal axis of (f) indicate the beginning of each year of simulation.

2.3 Data model comparison

ADCP observations from the PIRATA/EGEE campaigns (Fig. 1a) depict the EUC as a subsurface intensified jet at 6°E , immediately upstream of—and aligned with—São Tomé Island (Fig. 1b). The mean observed EUC flows at $0.42 \pm 0.2\text{ m s}^{-1}$, transporting 2.9 Sv within 120 m of water column, with its core at $66 \pm 15\text{ m}$ (for the ADCP diagnostics, the standard deviation is obtained from the different available transects at 6°E). Separated by the Equator, westward return flows appear centered at 1.8°N and 1.8°S (Fig. 1b). The NEMO 10-year mean (Fig. 1c) is consistent with the observed mean EUC, presenting only a slight overestimation in the core velocities, $0.45 \pm 0.11\text{ m s}^{-1}$ at $76 \pm 24\text{ m}$, with transport of $4.1 \pm 0.6\text{ Sv}$, and thickness of 130 m. The westward return flows appear smoothed due to the 10-year average, but present $0.23 \pm 0.06\text{ m s}^{-1}$ and $0.15 \pm 0.06\text{ m s}^{-1}$ (for the Northern and Southern Hemisphere, respectively) close to $90 \pm 40\text{ m}$. (In the model snapshots, core velocity reaches $> 0.7\text{ m s}^{-1}$ and the westward return flows reach $> 0.4\text{ m s}^{-1}$.)

224 Their position (1.5°N and 1.8°S) is also consistent with observations (Fig. 1b,c). The
225 EUC upstream of São Tomé in both ADCP and the model show values close to the ones
226 reported by Kolodziejczyk et al. (2014), who presented an observed mean velocity of 0.40 m s^{-1}
227 and mean transport of $3.7 \pm 2.5 \text{ Sv}$ at 6°E. From a single cruise (EGEE5, also used here
228 in our observations ensemble), the authors showed a 100-m-thick EUC, with its core at
229 70 m. The westward flows in Kolodziejczyk et al. (2014), evaluated at 2.3°E, are further
230 displaced from the Equator, at 2°N and 2.5°S. In our model, the westward jets centered
231 at 1.5°N and 1.8°S at 6°E move poleward, reaching 1.8°N and 2°S at 2.3°E.

232 To evaluate the modeled EUC vertical structure and salinity, we selected the point
233 closest to the PIRATA moored buoy (0°N, 0°E) in NEMO and interpolated the model
234 vertical levels into the PIRATA 5-m vertical grid. Our NEMO simulation performs sim-
235 ilarly to the salinity registered by the PIRATA buoy CTD (Fig. 1d), showing median
236 root-mean-squared differences (RMS) values of 0.23 between daily vertical profiles. (We
237 also calculated the correlation with the original PIRATA data, which yielded median val-
238 ues of 0.99, but only ~30% statistically significant correlations.) Overall RMS values (~80%)
239 below 0.3 indicate a good representation of the vertical salinity structure by the model.
240 With comparable mean and standard deviation, 35.6 ± 0.3 for the buoy (Fig. 1e) and 35.8 ± 0.5
241 for the model (Fig. 1f), the sharp contrast between surface low salinity and the high salin-
242 ity associated with the EUC is well captured by the model during the warm season (i.e.,
243 no upwelling), when the EUC is strongest. The equatorial upwelling season, which oc-
244 curs from May-June to August-September (see Picaut, 1983, and earlier references therein),
245 is known to weaken the EUC (e.g., Johns et al., 2014; Herbert et al., 2016) along with
246 its salt transport. The maxima in our model and buoy data are higher and the mean salin-
247 ity is slightly lower than in Kolodziejczyk et al.'s 2014 observations. This could be due
248 to their sampling periods over two separate months (June and September) outside the
249 period of a strongest EUC (December to May, Fig. 1e,f) and the peak of the equatorial
250 upwelling season in August (Jouanno, Marin, Du Penhoat, Sheinbaum, & Molines, 2011).

251 Particularly during the warm season, the model overestimates the vertical extent
252 of the strong subsurface salinity, but the model maximum salinity of 36.8 is consistent
253 with the buoy record of 36.7. In Figure 1d, sudden RMS peaks above 0.3 reveal that the
254 model struggles to fully represent the surface salinity increase due to vertical advection
255 at the beginning of the equatorial upwelling season (e.g. Jouanno, Marin, Du Penhoat,
256 Sheinbaum, & Molines, 2011; Da-Allada et al., 2017). Over time, an increasing salinity
257 trend in the model diverges from the CTD/buoy measurements, leading to an increas-
258 ing trend in the RMS values. This modeled salinity trend appears to be real, since there
259 were recent reports of a strengthening EUC in 23°W (e.g., Brandt et al., 2021; Stramma
260 & Schmidtko, 2021) that counteracts deoxygenation trends in the tropical Atlantic and
261 might explain the trend depicted from the model. However, for some unknown reason,
262 the PIRATA buoy failed to capture it. A thorough comparison of the EUC character-
263 istics between observations (ADCP and CTD/buoy), NEMO WI, and the literature (Kolodziejczyk
264 et al., 2014) is shown in Table 1.

Table 1. Summary of the comparison between observations (shipboard ADCP and the moored PIRATA buoy CTD), the NEMO reference (WI) numerical simulation, and observations reported by Kolodziejczyk et al. (2014). The CTD core depth is the depth of the maximum salinity.

EUC	Observations		NEMO	Kolodziejczyk et al. (2014)
	ADCP [6°E]	CTD [0°]		
velocity u [m s^{-1}]	0.42±0.2	—	0.45±0.1	0.40
transport [Sv]	2.9	—	4.1±0.6	3.7±2.5
thickness [m]	120	—	130	100
lat. westward flow [°N]	1.8	—	1.5–1.8	2.0
lat. westward flow [°S]	1.8	—	1.8–2.0	2.5
mean salinity	—	35.6±0.3	35.8±0.5	35.9
max. salinity	—	36.7	36.8	36.4
core depth [m]	60±15	50±14	76±24	70

265 The main features and dynamics of the eastern Gulf of Guinea are reasonably con-
 266 sistent between observations and model. Assured by the comparisons of this section, we
 267 next take advantage of the model’s spatial coverage and temporal resolution to track the
 268 EUC by its velocity, density limits, and remarkable salinity signal. We ask: what is the
 269 influence of the interaction between the EUC and the Gulf of Guinea islands on the re-
 270 gion’s meso-to-large-scale circulation? We start addressing the islands’ influence on the
 271 EUC bifurcation and, as we advance on Section 3, our findings motivate new analysis.

272 3 Meso-to-large-scale effects on the EUC circulation

273 To study the EUC across the tropical Atlantic basin, we focus on the isopycnal layer
 274 bounded on top by the 1025.3 kg m^{-3} and at the bottom by the 1026.4 kg m^{-3} isopyc-
 275 nals: the EUC layer. In the Gulf of Guinea between 0° and 6°E, the EUC layer contains
 276 the bulk of the EUC’s potential vorticity anomalies. For each model snapshot, we used
 277 the daily model density to delimit the EUC layer and performed a vertical average on
 278 each quantity for the grid points within this layer. Then, we time-averaged the individ-
 279 ual fields to obtain the mean isopycnal distributions. With our NEMO configuration,
 280 the EUC layer in the eastern Gulf of Guinea subset made possible a closer look at the
 281 role of the Gulf of Guinea islands in the bifurcation of the EUC, return flows, and as-
 282 sociated mesoscale dynamics at $\sim 9 \text{ km}$ resolution.

283 3.1 The bifurcation of the EUC

284 Islands in the Gulf of Guinea interact with the EUC circulation, affecting the dis-
 285 tribution of the high salt content brought by the EUC. Figure 2 displays a comparison
 286 between the WI and NI NEMO simulations, where the high salinity associated with the
 287 mean EUC pathways leaps off the page. For WI, Figure 2a shows the $>36 \text{ psu}$ salty tongue
 288 flowing at $\sim 0.5 \text{ m s}^{-1}$ eastward along the Equator; at 6.4°E, the EUC hits São Tomé Is-
 289 land, bifurcating into northbound and southbound branches. In the shadow zone formed
 290 between São Tomé and Príncipe Islands and the continental shelf, mean velocities are
 291 nearly zero, particularly in the Northern Hemisphere. But the salinity is relatively high
 292 in the shadow region, indicating salt dispersion by mesoscale activity besides the inter-
 293 mittent eastward advection (notably through the south of São Tomé) by the remnant
 294 EUC downstream of the islands in the Southern Hemisphere (Kolodziejczyk et al., 2014).

295 Nevertheless, the obstruction of the EUC flow by the islands partially separates the sub-
 296 surface high-salinity water from near-surface lower-salinity water—due to high precipi-
 297 tation (e.g., Houndegnonto et al., 2021), the Niger (e.g., Alory et al., 2021) and the Congo
 298 (e.g., Awo et al., 2018) river plumes—in the inner Gulf of Guinea, thus weakening the
 299 (already high) vertical salinity gradients that influence the surface water in the gulf through
 300 vertical advection (Awo et al., 2018). North and south of the Equator, westward return
 301 currents leave the domain at 0°E flowing centered at $\sim 2^\circ\text{N}$ and 2.5°S , which is consis-
 302 tent with observations discussed by Kolodziejczyk et al. (2014) at 2.3°E . Subsurface ob-
 303 servations in the EUC bifurcation are available mainly through the Argo array (Argo,
 304 2020) and Argo products, e.g., Roemmich and Gilson (2009)’s climatology (updated in
 305 2020), in which we were able to observe the bifurcation near São Tomé (not shown). The
 306 development and further analysis of such observations are important for a thorough char-
 307 acterization of the EUC termination site.

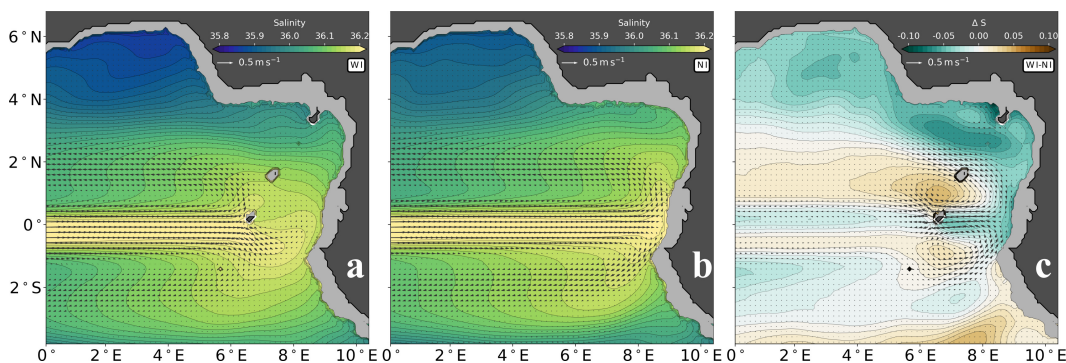


Figure 2. Mean NEMO salinity vertically averaged within the EUC layer ($1025.3\text{--}1026.4\text{ kg m}^{-3}$) for (a) the NEMO WI simulation, (b) the NEMO NI simulation, and (c) the difference WI minus NI. The gray shading represents the 100-m isobath. Arrows represent the mean horizontal velocity within the layer.

308 Without the islands (NI), Figure 2b depicts the EUC flowing past 6°E to termi-
 309 nate off the African continent at the Gabon coast. Curiously, the continental slope drives
 310 the EUC to bifurcate in a manner similar to the bifurcation caused by São Tomé in WI.
 311 In a model bi-monthly climatology representing the annual cycle of the bifurcation, Kolodziejczyk
 312 et al. (2014) showed a bifurcation of the EUC that resembled our NI simulation, with
 313 high salinity associated with the EUC often reaching Bioko Island, where the strongest
 314 differences appear in Figure 2c. This could be due to the simulation used by Kolodziejczyk
 315 et al. (2014), in which the islands do not seem to be well represented on their grid de-
 316 spite the $1/12^\circ$ horizontal resolution. The differences between the two models are com-
 317 plex to identify and the reasons behind these differences might include the bathymetry
 318 interpolation and smoothing, numerical schemes, atmospheric forcing, bulk formula, lat-
 319 eral boundary conditions, and others. In the NI simulation, the meridional spread of the
 320 high-salinity tongue is smaller in the region north and south of São Tomé, but the EUC
 321 penetrates further east, reaching the northeastern portions of the gulf (Fig. 2b,c). The
 322 westward flows also appear in both hemispheres, at latitudes close to those observed in
 323 WI and by Kolodziejczyk et al. (2014)’s observations and model.

324 Subtracting the salinity and horizontal currents of NI from the WI, Figure 2c shows
 325 a slightly weaker and fresher EUC in WI. Most important, it highlights the regions where
 326 the presence of islands impacts the general circulation. Due to the earlier bifurcation forced
 327 by São Tomé, which prevents the EUC from fully reaching the African continental slope,

328 the strongest differences are observed in the inner portions of the Gulf of Guinea, be-
329 tween Príncipe and Bioko Islands. In WI, the bifurcation at 6°E prevents high-salinity
330 waters from reaching the innermost portions of the gulf, with mean salinity anomalies
331 of -0.18 near Bioko Island and 0.18 near São Tomé related to the penetration of the EUC
332 in NI. North and south of São Tomé, an expected dipolar structure downstream of the
333 island appears with positive anomalies where the EUC bifurcates in WI. Following the
334 path of the westward flows, we note an interesting contrast in the large-scale pattern be-
335 tween hemispheres: the northern westward flow shows a positive salinity anomaly at around
336 2°N, whereas the southern flow shows a negative anomaly close to 2.5°S.

337 Zonal currents acting on strong horizontal salinity gradients play an important role
338 on the salt balance in different latitudes of the tropical Atlantic (e.g., Foltz et al., 2004).
339 For the Gulf of Guinea, even though the mean pattern points to a symmetric bifurca-
340 tion, the distinct anomalies hint at differences in the salt transport back to the western
341 tropical Atlantic. This north-south asymmetry is due mainly to the presence of the is-
342 lands in the Gulf of Guinea, as we will demonstrate by comparing WI and NI through-
343 out the manuscript. Nevertheless, other potential sources for the asymmetry may also
344 be present in the simulations, such as the wind forcing and the proximity from the con-
345 tinent and its geometry.

346 The termination of the EUC in the WI simulation in Figure 2a is analogous to the
347 Pacific EUC termination at the Galápagos Archipelago described from model analysis
348 (e.g. Karinauskas et al., 2007), ADCP data (e.g. Karinauskas et al., 2010), and glider ob-
349 servations (e.g., Jakoboski et al., 2020). In the Pacific, however, the bifurcation caused
350 by the islands continues flowing east, with most of the flow joining the continental slope
351 (cf. Karinauskas et al., 2007, 2010; Montes et al., 2010) toward both hemispheres. Here,
352 this is partially true for the Southern Hemisphere, where a remnant of the EUC flows
353 southeastward before veering west. However, for the Northern Hemisphere, the presence
354 of islands forces the flow westward, with no organized mean flow east of 6.5°E as seen
355 in NI. A major difference between the Atlantic and Pacific cases resides in the return flows.
356 Although they were also observed in the Pacific (e.g., Johnson et al., 2002), only a lesser
357 portion of the Pacific EUC veers west to support their formation (Karinauskas et al., 2007,
358 2010; Montes et al., 2010). In the Atlantic, these mean westward flows are a consequence
359 of the successive westward-propagating mesoscale eddies generated during the bifurca-
360 tion of the EUC in the inner portions of the Gulf of Guinea (Assene et al., 2020).

361 We showed how the islands (particularly São Tomé) block the EUC, preventing salty
362 waters to reach the innermost portions of the gulf. At a first glance, no remarkable change
363 in the returning westward flows were observed, since the bifurcation also occur in NI,
364 which leads us to question: does the presence of islands only impact the circulation lo-
365 cally, or are there consequences to the net fluxes across the Atlantic? To answer this ques-
366 tion, we further explore the role played by islands in the EUC bifurcation and westward
367 returning flows. To better track the origin of the bifurcation and eddies, as well as the
368 changes undergone by the EUC during eddy formation, we perform a PV analysis in the
369 EUC layer, focusing on the eastern portions of the Gulf of Guinea.

370 3.2 Gulf of Guinea islands and mesoscale dynamics of the EUC

371 Potential vorticity is a key quantity in the interpretation of ocean dynamics due
372 to its strong link with circulation, conservation along isopycnals, and inversion proper-
373 ties (Bretherton & Haidvogel, 1976; Hoskins et al., 1985; Morel et al., 2019). Accord-
374 ing to Rhines (1986), geostrophic turbulence develops regions of homogenized PV and
375 specific circulation patterns. In quasigeostrophic models, this circulation is fundamen-
376 tally associated with the PV anomaly, calculated with respect to a background PV at
377 rest. Since this background PV—simply equal to the Coriolis parameter for the quasi-
378 geostrophic model—varies spatially with latitude, meridional advection can lead to lo-

379 cal PV anomalies and alter the circulation. Indeed, there is a quantitative link between
 380 the integrated PV anomaly and the barotropic circulation or transport (e.g., Morel et
 381 al., 2019). While PV is conserved for adiabatic evolution, friction and diapycnal mix-
 382 ing can in turn modify the PV and create anomalies, generating circulation patterns. In
 383 the present study, we analyze the differences between the WI and NI circulations through
 384 their PV structures.

385 In the study of equatorial zonal jets, the well-known PV structure is characterized
 386 by a meridional inversion of homogeneous PV and strong gradients at each side of the
 387 jets (cf., Fofonoff & Montgomery, 1955; Pedlosky, 1987; Pedlosky & Spall, 2015). Along
 388 the Equator, low-PV waters and weak zonal gradients characterize the core of the flow
 389 (e.g., Ménesguen et al., 2009; Delpech et al., 2020). Usually, PV within the pycnocline
 390 is dominated by the strong background signal of the stratification at rest, making it dif-
 391 ficult to distinguish horizontal anomalies related to the “dynamically-active” PV (e.g.,
 392 eddies). To overcome this limitation, Morel et al. (2019) proposed an alternative calcu-
 393 lation for PV, in which a rescaling allows the interpretation of the evolution of PV anom-
 394 alies along isopycnic surfaces, as proposed by Hoskins et al. (1985). The rescaled PV has
 395 the same conservation properties as the Ertel PV—boiling down to the quasigeostrophic
 396 PV when geostrophic and hydrostatic approximations are made—but compensates for
 397 the signature of the pycnocline that would otherwise dominate the Ertel PV. Previously
 398 used by Delpech et al. (2020) and Assene et al. (2020) in the study of equatorial jets,
 399 Morel et al.’s (2019) rescaled PV,

$$Q = (\boldsymbol{\zeta} + \mathbf{f}) \cdot \nabla G_\rho, \quad (1)$$

400 is obtained using a specific function G_ρ based on potential density and chosen so that
 401 for all density levels the PV at rest associated with a reference density profile is equal
 402 to the vertical component of the planetary vorticity. In (1), $\boldsymbol{\zeta}$ and \mathbf{f} are the 3D relative
 403 vorticity and Earth rotation vector, respectively. In considering primitive equations, we
 404 neglect the vertical velocity terms in $\boldsymbol{\zeta}$ and use only the vertical component of \mathbf{f} , i.e., the
 405 Coriolis parameter $f = 2\Omega\sin(\varphi)$ —where φ is the latitude and $\Omega = 7.29 \times 10^{-5} \text{ s}^{-1}$ —
 406 and $\boldsymbol{\zeta} = (-\partial_z v, \partial_z u, \partial_x v - \partial_y u)$. G_ρ is the rescaling function responsible for masking
 407 the background stratification effect on PV (cf. Morel et al., 2019). It is based on a ref-
 408 erence density profile representative of the PV at rest and has units of meters. To ob-
 409 tain this reference density ρ_r , we tested several density profiles aiming to reduce the ef-
 410 fect of stratification on PV, and chose a 10-year mean profile averaged in a 0.5° box around
 411 ($1.5^\circ\text{N}, 8.5^\circ\text{E}$), so $\rho_r = \overline{\langle \rho \rangle}$. The area is close to the choice for reference profile by
 412 Assene et al. (2020) using a similar NEMO configuration. Unlike Assene et al. (2020),
 413 we opt here for a spatio-temporal-averaged profile which nevertheless presents the de-
 414 sired characteristics for rescaling the PV, such as low surface densities and stratification
 415 typical of the pycnocline at rest (Morel et al., 2019; Assene et al., 2020).

416 The mean horizontal distribution and standard deviation of the PV in the EUC
 417 layer is displayed in Figure 3. Away from the continent (i.e., from ~ 0 to 5°E), both WI
 418 and NI simulations show the inversion in PV typical of equatorial jets (Fig. 3a,b): from
 419 the Southern Hemisphere ($\sim 1^\circ\text{S}$) to the north, PV is negative and increases northward,
 420 crossing the low PV band ($Q \approx 0$) around the Equator to show strong positive values
 421 at $\sim 1^\circ\text{N}$. Approaching 6°E , however, Figure 3a displays the bifurcation of the low-PV
 422 waters ($|Q| < 0.6 \times 10^{-5} \text{ s}^{-1}$) associated with the core of the EUC (and also with the
 423 maximum salinity region in Fig. 2a) and their spread across the shadow area downstream
 424 of the islands. The presence of São Tomé Island also acts to redirect the low PV of the
 425 EUC southeastward, forming a meander before reaching the African coast. In the lee of
 426 São Tomé, weak mean velocities and high variability point to transient mesoscale fea-
 427 tures playing a major role in spreading the EUC low PV eastward (also shown in the PV
 428 animations available in this study’s supplementary information S2). Moreover, positive
 429 anomalies east of the island ($0^\circ\text{N}, \sim 7^\circ\text{E}$) and patches of weaker negative anomalies north

430 and northeast of the island ($\sim 1^\circ\text{N}$, $\sim 7^\circ\text{E}$) show local PV anomalies due to interaction
 431 between the EUC and São Tomé. Thus the PV variability account for both adiabatic
 432 (change of path of the current imposed by kinematic boundary conditions) and diabatic
 433 (friction and mixing close to the islands) effects. As described in Figure 2b, the bifur-
 434 cation in NI occurs at the continental slope; the zonal spread is smaller, but the low-PV/highest-
 435 salinity waters reach the innermost portions of the gulf (Fig. 3b). As seen in the differ-
 436 ence between WI and NI (Fig. 3c), the mean effect of the islands on the PV is the pres-
 437 ence of PV dipoles in the vicinity of the islands (e.g., Pedlosky & Spall, 2015). The biggest
 438 structure is located downstream of São Tomé, but similar features can be seen near Príncipe,
 439 Bioko or even Annobón (2°S , $\sim 6^\circ\text{E}$).

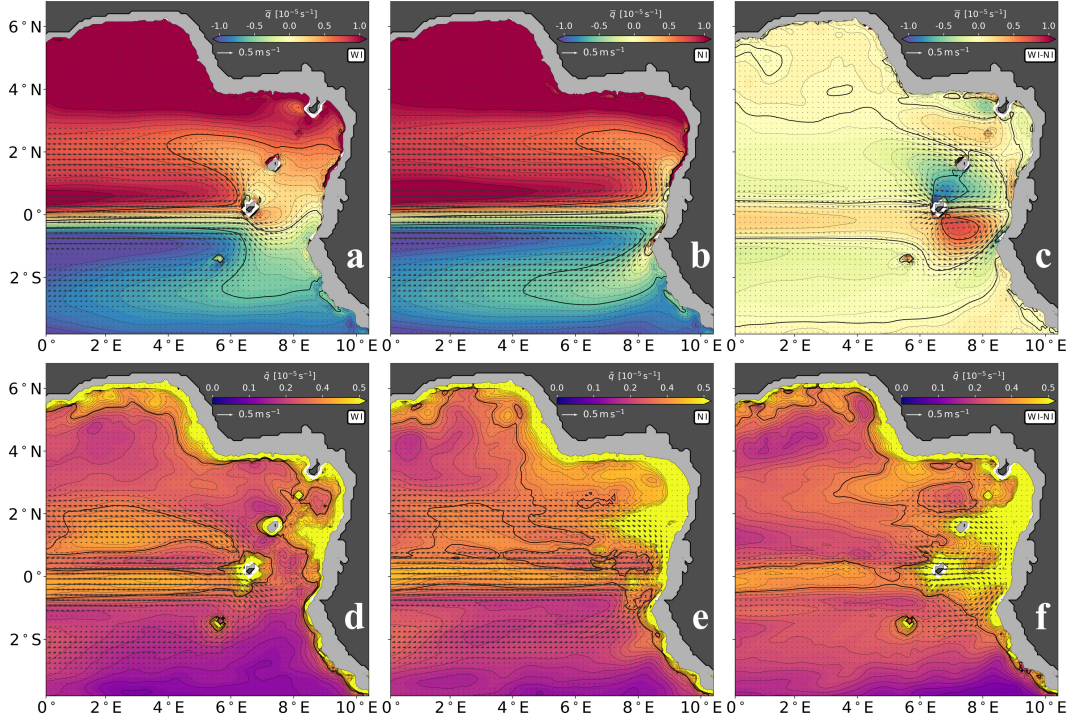


Figure 3. PV in NEMO experiments. (a-c) Mean PV vertically averaged within the EUC layer ($1025.3\text{--}1026.4 \text{ kg m}^{-3}$) for the WI simulation (a), the NI simulation (b), and the difference between WI and NI (c). Thick black lines represent $|Q| = 0.6 \times 10^{-5} \text{ s}^{-1}$. The gray shading represents the 100-m isobath. Arrows represent the mean horizontal velocity within the layer. (d-f) PV standard deviation within the EUC layer for WI (d), NI (e), and the difference between WI and NI (f). Thick black lines represent the standard deviation of $0.35 \times 10^{-5} \text{ s}^{-1}$.

440 Away from the Gulf of Guinea, in both experiments, two PV tongues extending
 441 westward from their respective bifurcation sites indicate the main fate of the EUC wa-
 442 ters (Fig. 3a,b). As previously reported, the PV tongues are a reflex of the current ter-
 443 mination in a bifurcation (Kolodziejczyk et al., 2014) and the formation of westward-
 444 propagating mesoscale anticyclonic eddies (Assene et al., 2020). The remarkable obser-
 445 vation here is the westward extension of the strong low-PV signal, which shows an asym-
 446 metry between the WI and NI experiments. In Figure 3a, the Northern Hemisphere $|Q| < 0.6 \times$
 447 10^{-5} s^{-1} tongue reaches 4°E , while its Southern Hemisphere counterpart stops at $\sim 6^\circ\text{E}$.
 448 The opposite is observed in the NI case (Fig. 3b), which is consistent with differences

449 between the simulations in respect to the saltier waters advected westward by the ed-
450 dies noted in Figure 2c.

451 The temporal variability of PV (Figs. 3d–f) shows a zonal band of relatively high
452 variations in PV along the Equator. Part of this variability is adiabatic and does not nec-
453 essarily indicate PV transformation. Instead, these variations may occur due to seasonal
454 and interannual latitudinal migration of the main axis of the EUC (Jouanno et al., 2013;
455 Brandt et al., 2014). Studying the seasonality of the surface cooling in the Gulf of Guinea
456 with a numerical model, Jouanno et al. (2013) noted this EUC core meridional migra-
457 tion. Later, using mooring and shipboard velocity measurements and an EOF analysis,
458 Brandt et al. (2014) identified latitudinal excursions of the EUC core, represented by both
459 southward and northward anomalous displacements. The authors linked this process to
460 an interannual variability, consistent with the timescale of the variability of basin-mode
461 oscillations due to the eastward propagation of equatorial Kelvin waves and the rebound
462 of westward long equatorial Rossby waves [cf. Cane and Moore (1981); see also Brandt
463 et al. (2011)]. However, intermittent processes also play a role, with friction and diapy-
464 cnal mixing being able to drastically modify the PV distribution within an oceanic cur-
465 rent (e.g., Morel & McWilliams, 2001). In particular, the strongest PV variations in Fig-
466 ures 3d–f occur near topography, with clear hotspots of variability around the islands
467 (Fig. 3d). These locations might indicate sites of diabatic PV transformation. There,
468 friction likely plays a major role in transforming PV (e.g., D’Asaro, 1988; Morel & McWilliams,
469 2001; Benthuisen & Thomas, 2012), but we acknowledge that staircase bottom and lat-
470 eral walls (as well as wind stress, to a lesser extent at the EUC depth, ~ 80 m) in the model
471 may add to this effect. In Figure 3d, an east-west band of high PV variation between
472 1 and 2°N points to São Tomé as the source of this variability, although its presence also
473 in NI (Fig. 3e) prevents us from pinpointing its association with the islands.

474 The PV maps in Figure 3d,e hint at flow-topography interactions as a major pro-
475 cess responsible for creating PV anomalies in both simulations, whether with the islands
476 in WI or the African continent in WI and NI. In terms of the mean circulation pattern
477 (Fig. 3), friction with land generates anticyclonic PV anomalies. Indeed, Assene et al.
478 (2020) showed that anticyclonic eddies generated from PV anomalies in the Gulf of Guinea
479 propagate west through the tropical Atlantic in eddy corridors between 4°S and 4°N.
480 However, local friction effects at shorter time scales are far more complex—generating
481 both anticyclonic and cyclonic anomalies—and should not be estimated solely from Fig-
482 ure 3, which leads us to question: do EUC-islands interactions (particularly São Tomé)
483 play a role in the formation and distribution of such eddies? Moreover, can these inter-
484 actions shape the EUC return flows and transform its PV?

485 3.3 Extra-equatorial westward-propagating eddies

486 In the Gulf of Guinea, the EUC arriving at the easternmost portions of the gulf
487 triggers the formation of mesoscale anticyclones that propagate westward, toward the
488 direction of the incoming flow (e.g., Assene et al., 2020). A sequence of PV snapshots
489 in Figure 4 illustrates the extra-equatorial eddy corridors during a period of strong eddy
490 activity. In both simulations, anticyclonic eddies are formed in both hemispheres and
491 propagate westward at $\sim 0.11 \text{ m s}^{-1}$ (10 km day^{-1}). However, comparing the eddies in
492 WI and NI, differences in their size and strength can be depicted. On 27 Dec 2007, Fig-
493 ure 4a captures an anticyclone organizing at 5°E northwest of the Gulf of Guinea islands;
494 at $\sim 1^\circ\text{E}$, a pinched-off eddy propagates westward, with a trail of low PV suggesting de-
495 formation due to lateral shear between the eddy and the EUC. In the Southern Hemi-
496 sphere, a weaker low-PV signal leaves the region at $\sim 2^\circ\text{S}$. The following snapshots, af-
497 ter 30 and 60 days (Figures 4b,c, respectively), show the evolution of the flow, with strong
498 ~ 100 -km-radius eddies traveling in the north corridor, and smaller, faint eddies occur-
499 ring in the Southern Hemisphere. In the NI simulation, the EUC still bifurcates, but its
500 bifurcation occurs at the African continental slope rather than at $\sim 6^\circ\text{E}$. Figure 4d shows,

501 in both hemispheres at $\sim 8^\circ\text{E}$, the nearly symmetric formation of eddies which propa-
 502 gate westward at velocities similar to those in WI. However, in NI the larger and stronger
 503 eddies appear in the Southern Hemisphere (Fig. 4e,f). This eddy-formation pattern is
 504 recurrent throughout the model timeseries, as discussed below.

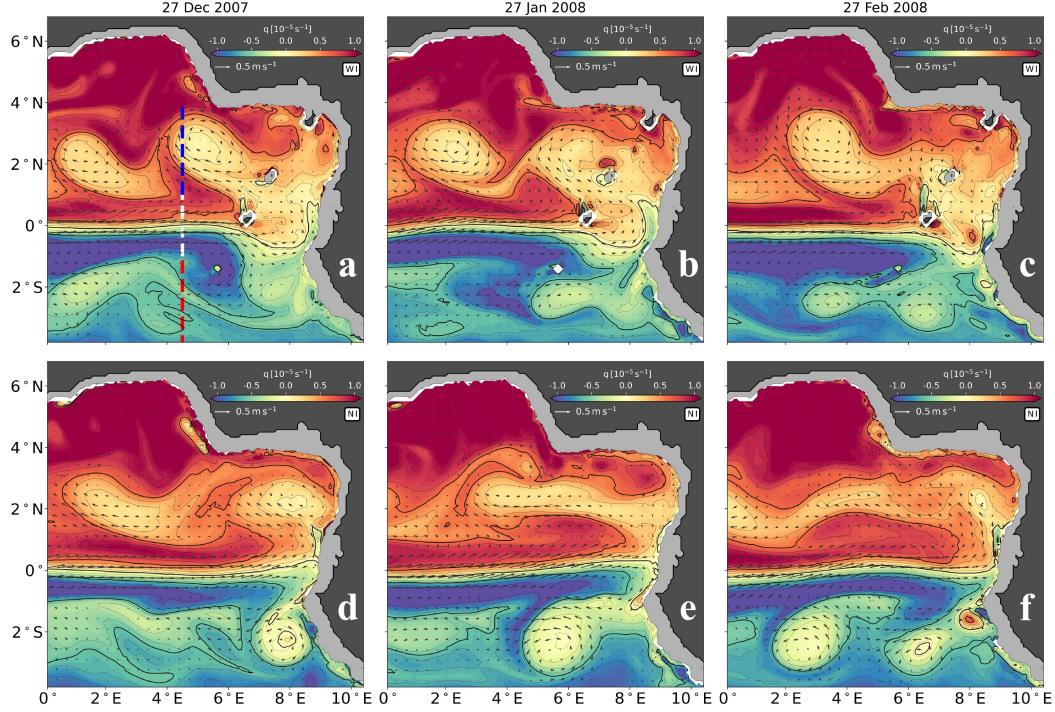


Figure 4. Snapshots of NEMO PV vertically averaged within the EUC layer ($1025.3\text{--}1026.4\text{ kg m}^{-3}$) for the (a-c) NEMO WI simulation and (d-f) NEMO NI simulation. (See animations in the supporting information of this paper.) Thick black lines represent $|Q| = 0.6 \times 10^{-5}\text{ s}^{-1}$. The gray shading represents the 100-m isobath. Arrows represent a subset of the horizontal velocity vertically averaged within the layer. The meridional section in (a) is used to quantify the PV and salt fluxes in the Equator (white) and North (blue) and South (red) Hemispheres.

505 To better compare the evolution of the flow in WI and NI, we analyze the meridional
 506 structure of the PV together with the energy associated with eddies. We distinguish
 507 the low-PV regions (regardless of the PV sign) and their associated eddy activity
 508 by calculating the longitudinally averaged, meridional profiles of the potential enstrophy
 509 (Q^2) and eddy kinetic energy ($\text{EKE} = \tilde{u}^2 + \tilde{v}^2$, where the tilde represents the anomaly
 510 from a low-pass filter of 60 days) of the EUC. Figure 5 shows the median values of EKE
 511 (Fig. 5a) and Q^2 (Fig. 5b) meridional profiles for WI superimposed on NI, in zonally
 512 averaged bands spanning 3° from 0° to 9°E . Between $1^\circ\text{S}\text{--}1^\circ\text{N}$, both simulations show
 513 nearly coincident high EKE and low enstrophy (and consequently low PV) from 0° to
 514 6°E , with two local maxima around a local minimum at 0° . In the easternmost profile,
 515 this pattern is less evident but still present in NI's Q^2 (Fig 5b), while in EKE and in WI's
 516 Q^2 the pattern collapses due to the bifurcation. The low PV extends to about 2° meridionally
 517 from the Equator, developing local PV anomalies with respect to the higher PV
 518 background at $\sim 2^\circ\text{N}$ and 2°S . The roll up of these low-PV anomalies into eddies occurs
 519 in both simulations, but at different longitudes. Nevertheless, they propagate westward

520 through the same eddy corridors, centered at $\sim 2^\circ$ on both sides of the Equator. This
 521 allows a qualitative comparison between the EKE maxima associated with a Q^2 min-
 522 ima in both hemispheres. The median values of WI in Figure 5 show higher values of
 523 EKE and smaller values of Q^2 in the return flow north of the Equator compared to NI,
 524 while the opposite [i.e., NI's EKE (Q^2) greater (smaller) than WI] is observed south of
 525 the Equator.

526 Considering that the incoming EUC has virtually the same EKE and Q^2 in both
 527 experiments, the median difference implies that in WI, stronger eddies carrying more low-
 528 PV are generated in the Northern Hemisphere than in the Southern Hemisphere and that
 529 the opposite is true in NI. An overlap within 60% of the EKE and Q^2 distributions (0.2
 530 and 0.8 quantiles) between the two simulations is consistent with the recurrent presence
 531 of low-PV eddies in both hemispheres for WI and NI; their presence in both simulations
 532 further points to stronger eddies responsible for the north-south asymmetry around 2°N
 533 and 2°S (Fig. 5a,b). This asymmetry could be due to the suppression of symmetric in-
 534 stability modes in the presence of islands, one of the distinct unstable modes that lead
 535 to eddy formation in the EUC (e.g., McCreary & Yu, 1992).

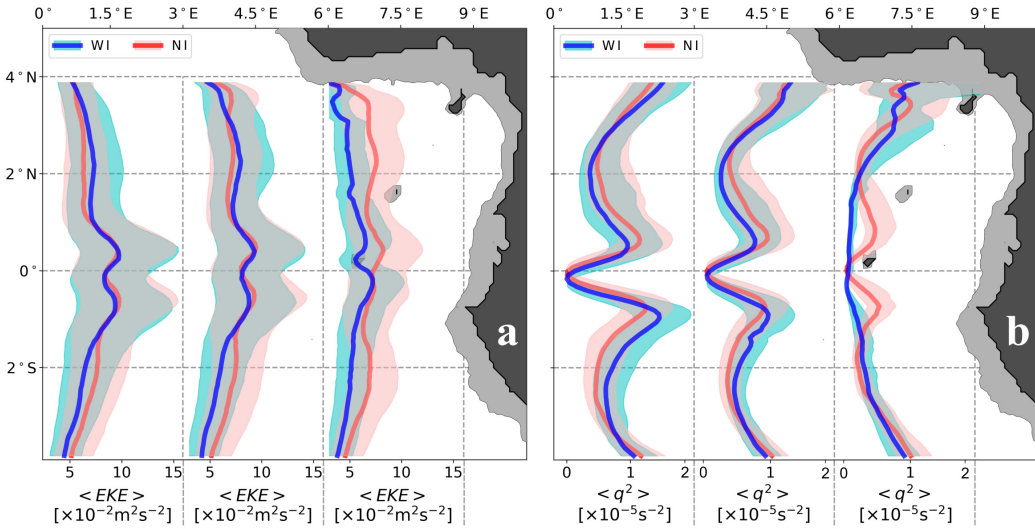


Figure 5. Zonally averaged (a) eddy kinetic energy and (b) potential enstrophy profiles within the EUC layer ($1025.3\text{--}1026.4 \text{ kg m}^{-3}$) between $0\text{--}3^\circ\text{E}$, $3\text{--}6^\circ\text{E}$, and $6\text{--}9^\circ\text{E}$. Lines represent the median values for the NEMO WI (blue) and the NEMO NI (red) simulations. The light blue and light red bands around the lines represent the interval between the 0.2 and 0.8 quantiles.

536 Below, we investigate how the interaction between the Gulf of Guinea islands and
 537 the EUC dynamics is responsible for the apparent difference in eddy generation between
 538 hemispheres depicted in Figures 3 to 5. For the meridionally-alternating flows associ-
 539 ated with the EUC, we calculated the PV and salinity fluxes across a meridional section
 540 at 4.5°E (see the meridional transects in Fig. 4a). The transects span $1^\circ\text{S}\text{--}1^\circ\text{N}$, $1\text{--}4^\circ\text{S}$,
 541 and $1\text{--}4^\circ\text{N}$ for the Equator, southern, and northern paths, respectively. For the flux Φ
 542 of a quantity A advected across these meridional sections,

$$\Phi = \iint_S (uA) dydz, \quad (2)$$

543 u is the zonal velocity crossing the section within a low-PV region, and dy and dz are
 544 the “steps” in latitude and depth range of the meridional section. In this analysis, y varies
 545 for the Equator, south, and north sections at 4.5°E as described above. The thickness
 546 z is the distance between the isopycnals of the EUC layer. We restricted the analysis to
 547 the EUC core ($1025.3\text{ kg m}^{-3} < \rho < 1026.4\text{ kg m}^{-3}$) and the PV anomalies that origi-
 548 nated from this waters; in practice, outside the region of low PV ($|Q| < 0.6 \times 10^{-5}\text{ s}^{-1}$),
 549 we set the velocity $u = 0$. With u representing only the low-PV flow and zero elsewhere,
 550 we use (2) with $A \equiv \rho S_a$ (S_a : absolute salinity) and $A \equiv Q$ to obtain the salt and
 551 PV fluxes, respectively.

552 The EUC advects salt into the Gulf of Guinea by carrying SMW and SACW from
 553 the western tropical Atlantic (e.g., Stramma & Schott, 1999). Within its core, the high-
 554 est values of salinity are associated with low values of PV, which are also related to the
 555 PV anomalies that form the westward-traveling mesoscale eddies (Fig. 4). At these depths,
 556 the connection between the western and eastern sides of the tropical Atlantic is thus domi-
 557 nated by—but not restricted to—the eastward and westward fluxes within the low-PV
 558 band of the EUC. For the incoming EUC, Figure 6a shows similar incoming fluxes for
 559 both WI and NI, with the EUC advecting on average $93 \pm 39 \times 10^6\text{ kg s}^{-1}$ into the do-
 560 main between 1°S and 1°N , with peaks above $150 \times 10^6\text{ kg s}^{-1}$ (maximum $212 \times 10^6\text{ kg s}^{-1}$).
 561 These peaks show an ~ 120 -day variability, consistent with the period of equatorial Kelvin
 562 waves at this depth (e.g., Polo et al., 2008; Bachèlery et al., 2016; Illig & Bachèlery, 2019).
 563 The effect of Kelvin waves can be crucial to deepen the EUC core by modifying the ther-
 564 mocline slope (Hormann & Brandt, 2009), thus affecting the depth at which the EUC
 565 hits the island. As a consequence, the flow meets a larger bathymetric signature of the
 566 island, and flow-island interactions tend to strengthen (recall the model island’s bathymetry
 567 from Fig. 1). Figures 6b and c show the westward salt flux between $1\text{--}4^\circ\text{N}$ and $1\text{--}4^\circ\text{S}$,
 568 respectively. In both cases, we observe strong variability, with peaks in the salt flux in-
 569 terposed with periods of zero transport, consistent with the intermittent passage of low-
 570 PV vortical structures. In the Northern Hemisphere (Fig. 6b), transport peaks due to
 571 eddies are stronger in the WI simulation, whereas in the Southern Hemisphere (Fig. 6c),
 572 the peaks due to mesoscale eddies appear mainly in the NI simulation. Time-integrating
 573 (2) for the 10-year time series yield a total salt input of $\sim 30\text{ Eg}$ ($1\text{ Eg} \equiv 1\text{ exagram} =$
 574 10^{15} kg). *That is equivalent to more than 50 million RMS Titanics fully loaded with salt*
 575 *travelling from west to east and back every year!* (Or about 6 million times the capac-
 576 ity of the largest modern container ships.) After the incoming EUC breaks up into westward-
 577 propagating anticyclonic eddies, the WI salt flux integrated on the north corridor accounts
 578 for $47 \pm 5\%$ of the influx, and the south path transports only $23 \pm 4\%$ (orange lines in
 579 Fig. 6b,c). In NI, the asymmetry is virtually nonexistent, with $39 \pm 5\%$ of the incom-
 580 ing flow returning west through the north corridor and $32 \pm 2\%$ through the south cor-
 581 ridor (cyan lines in Fig. 6b,c).

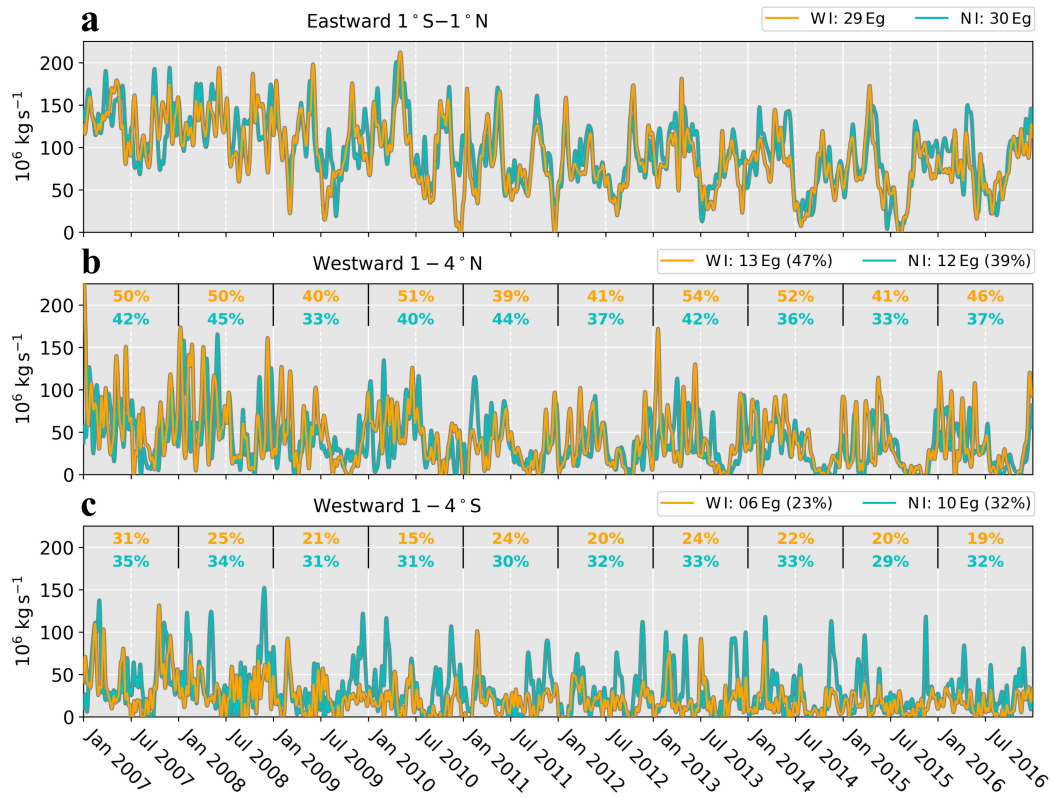


Figure 6. Low-pass filtered (7 days) daily salt fluxes at 4.5°E for the (a) eastward-flowing EUC between 1°S and 1°N , (b) Northern Hemisphere westward return flow between 1 and 4°N , and (c) Southern Hemisphere westward return flow between 1 and 4°S . Orange lines represent the WI simulation, and cyan lines represent the NI simulation. The legend boxes show the integrated transport for the 10-year model series in Eg (exagram = 10^{15} kg), with yearly percentages of westward transport (b,c) relating the transport in each hemisphere to the total eastward transport at the Equator for the period.

The difference between the north and south corridors goes beyond the percentages of return flux expressed above. In Figures 6b,c, peaks related to eddies in NI present comparable formation periods and strength for both hemispheres. For WI, however, differences in the number and strength of the eddies between hemispheres appear: while weak and rare in the Southern Hemisphere, eddies in the north corridor are numerous and grow much stronger. The distribution of the peaks in Figures 6b,c shows that eddies also present seasonal and interannual variability related to the EUC's variability depicted in Figure 6a.

Every year, eddies are generated preferentially from December to June (Fig. 6b). This aligns with the notion that a strong EUC is essential to the formation of the anticyclonic eddies, seeing that, from June to November, the equatorial upwelling season weakens the EUC (e.g., Jouanno et al., 2013; Johns et al., 2014; Herbert et al., 2016) and eddy occurrence is smaller (Fig. 6b,c). Moreover, the strongest eddies in the model occur in WI for the Northern Hemisphere, where a strong EUC interacts with São Tomé. Particularly in 2008, 2009, and (less evident in) 2013, the strongest events in WI ($>100 \times 10^6 \text{ kg s}^{-1}$; Fig. 6b) stand out from the series. This is probably due to the northward shift of the EUC at 6°E during these periods, which is consistent with strong flow-island interactions

(note in our model's PV animation S2 that São Tomé Island is located somewhat on the northern side of the equator). Such meridional displacements of the EUC are due to the current's interannual variability (e.g., Brandt et al., 2014). The meridional shift in our simulation is opposite to that which Brandt et al. (2011) reported at 23°W (southward). At 6°E, where São Tomé Island is, the shift is indeed opposite to Brandt et al's.

Taking N_c and S_c as the salt transported westward through the north and south corridors (Fig. 6b,c, respectively), we can quantify the EUC split between hemispheres:

$$\sigma = \frac{N_c}{N_c + S_c}. \quad (3)$$

In the WI simulation, $\sigma_{WI} \approx 2/3$ indicates that the asymmetry imposed by the islands is quantitatively significant. In the absence of islands, $\sigma_{NI} \approx 1/2$ points to a symmetric bifurcation at the African continental slope, with westward flows mirrored by the Equator. Another simple yet useful relation,

$$\lambda = \frac{N_c + S_c}{I_e}, \quad (4)$$

accounts for the loss of the incoming EUC (I_e) waters within the innermost portions of the Gulf of Guinea. The ratio (4) $\lambda_{WI} \approx \lambda_{NI} \approx 0.7$ indicates a 30% loss of salt content in both simulations. Possible reasons accounting for this imbalance include fluxes of EUC waters to higher latitudes and diapycnal mixing, which leads to exchanges between the upper and lower layers. As far as PV fluxes are concerned, the advection of PV anomalies by westward-propagating eddies (not shown) follows the same pattern as salinity (with opposite sign on the Southern Hemisphere), which is not surprising, since PV and salinity are somewhat homogeneous within the eddies.

The variability of the EUC and its interaction with the islands of the Gulf of Guinea introduce an asymmetry to the transport of tracers via eddy corridors in the Northern and Southern Hemispheres. This occurs mainly due to the formation of stronger and more numerous eddies in the Northern Hemisphere in WI. Moreover, salinity and PV, as they are transported by those eddies, are also modified within the Gulf of Guinea. While changes in the salinity are only due to mixing, PV is also modified by friction, which is now used to separate the influence of both effects on the PV diabatic evolution. Finally, both processes being strengthened locally around the islands, we are encouraged to focus on the encounter between the EUC and São Tomé, where regional processes comes into play in the transformation of the EUC waters during the current's bifurcation and eddy generation.

4 Changes in the EUC around the Gulf of Guinea islands

During bifurcation, the EUC naturally generates eddies with or without islands due to different unstable modes (e.g., McCreary & Yu, 1992). Flow-topography interactions can change this instability, being responsible for the generation of mesoscale features (e.g., Jouanno & Capet, 2020) that escalates to alter larger-scale dynamics through geostrophic turbulence and the inverse energy cascade (cf. Charney, 1971; Hoskins et al., 1985). An eddy carrying a PV anomaly from east to west in an ocean basin translates into an input of eddy kinetic energy proportional to the eddies' enstrophy (e.g., Li et al., 2018). In the Gulf of Guinea, the propagation of these low-PV eddies introduces PV anomalies that affect the dynamics throughout their westward paths in the tropical Atlantic. Therefore, in this section, we use PV diagnostics to infer how diapycnal mixing or other mechanisms (such as friction and isopycnal mixing) can modify the EUC waters, and we propose a rough estimation of their effects. We first evaluate the mean PV of parcels entering the area within the EUC and then leaving in the core of eddies, forming the north

643 and south return flows. Modification of this quantity is necessarily associated with di-
 644 abatic effects. To evaluate the diapycnal fluxes in and out of this layer causing the PV
 645 modification, we note that the volume of the EUC layer varies only because of diapy-
 646 cnal mixing, since isopycnal mixing does not change the EUC layer volume bounded by
 647 two isopycnal levels. These fluxes can be used to infer the effect of diapycnal mixing on
 648 PV, with the remaining PV changes being accounted for other processes (friction and
 649 mixing along isopycnal surfaces). Finally, since the dynamics and the vorticity of eddies
 650 reflect the PV anomaly (with respect to the local planetary vorticity for the rescaled PV),
 651 meridional displacements have to be considered, too.

652 4.1 PV anomalies in the EUC

653 In our modeled EUC in the eastern Gulf of Guinea, local PV anomalies can derive
 654 from meridional advection of PV, with low-PV EUC waters moving into a high-PV back-
 655 ground due to the bifurcation of the EUC, leading to positive and negative anomalies
 656 in the Southern and Northern Hemispheres, respectively (e.g., Assene et al., 2020, see
 657 also Fig. 4). Due to conservation of PV, these opposite PV anomalies in different hemi-
 658 spheres will develop an anticyclonic circulation proportional to the strength of the merid-
 659 ional displacement (Morel et al., 2019; Assene et al., 2020). Local effects of friction and
 660 diapycnal and/or isopycnal mixing also change the PV distribution (e.g., Morel & McWilliams,
 661 2001). In the present study, the estimation of PV and salinity fluxes gives us some in-
 662 dications about the processes involved in the generation of eddies and modification of
 663 the circulation in the vicinity of the islands. Indeed, in an isopycnal layer, mixing and
 664 friction are both important to generate PV anomalies that develop into eddies.

665 The PV evolution equation for each Lagrangian particle is a combination of advec-
 666 tion, diapycnal mixing, and friction terms (Müller, 2006, see also, e.g., Thomas, 2005,
 667 and Gula et al., 2019). Cast in the Eulerian form,

$$\partial_t Q = - \operatorname{div} \left(\underbrace{\mathbf{u} Q}_{\text{advection}} + \underbrace{\nabla G_\rho \times \mathbf{F}}_{\text{friction}} - \underbrace{(\boldsymbol{\zeta} + \mathbf{f}) \frac{dG_\rho}{dt}}_{\text{diapycnal mixing}} \right), \quad (5)$$

668 the PV evolution is the sum of the individual terms in the right-hand side of (5), where
 669 \mathbf{u} is the advection velocity, \mathbf{F} represents friction and other nonconservative forces (e.g.,
 670 Thomas, 2005; Gula et al., 2019), and dG_ρ/dt accounts for diapycnal mixing effects. To
 671 obtain rigorous quantitative budgets of (5), we need daily diapycnal mixing and friction
 672 terms for each particle. Although this is not possible in the present experiments, qual-
 673 itative estimates of PV transformation within the Gulf of Guinea can be drawn from the
 674 following approach and assumptions:

- 675 • the mean flow (over the 10 years of simulation) is constrained within Northern and
 676 Southern Hemisphere streamtubes of volume V , connecting the northern and south-
 677 ern exit sections to entrance sections within the EUC. The streamtube is bounded
 678 vertically by the EUC layer and laterally by mean circulation streamlines;
- 679 • for each streamtube, we assume the initial/entrance PV can be estimated using
 680 the mean PV over their respective EUC section (even though the streamtubes may
 681 represent only a fraction of the EUC section);
- 682 • volume variations within each streamtube are predominantly due to diapycnal fluxes,
 683 while lateral fluxes are negligible (as shown in Figs. 2 and 3, mean velocities are
 684 weak at the edge of the streamtube, with associated fluxes representing less than
 685 5% of the EUC incoming fluxes);
- 686 • the incoming EUC transport V_{EUC} to each hemisphere follows the same ratio as
 687 the split between hemispheres at the exit (i.e., Equation 3 applied to the volume
 688 flux instead of salinity). This is a rough approximation, but sufficient to get an
 689 order of magnitude for the effect of diapycnal mixing on the PV budget.

The approach and assumptions above (detailed in the supplementary information S3) allow us to use mean volume flux to estimate the changes in the mean PV values of the EUC. The mean values are defined by dividing the PV flux by the volume flux to obtain average values entering and leaving the domain through the streamtubes. For the flow that returns westward, the final mean PV advected at the exit section is thus the initial mean PV plus anomalies imposed by diapycnal mixing and other processes, which include friction and isopycnal mixing (and also possible effects due to wave-flow interaction and errors associated with numerical schemes and with the diapycnal mixing estimation). At the exit section,

$$Q_f = Q_{\text{EUC}} + \delta Q_{\text{mix}} + \delta Q_{\text{other}}, \quad (6)$$

where Q_{EUC} is the mean EUC PV at the Equator and Q_f represents the mean outgoing PV, with $Q_f = Q_N$ and Q_S for the northern and southern streamtubes, respectively.

We consider eastward-flowing water columns with mean Q_{EUC} bifurcating in the east Gulf of Guinea (Fig. 7a). In our assumptions, the incoming Q_{EUC} has different values for each hemisphere/streamtube; at these locations, δQ_{mix} and δQ_{other} modify the incoming PV independently. The PV transformation due to diapycnal mixing is a function of the initial PV and the volume change (see Haynes & McIntyre, 1987, and section S3 in the Supporting Information),

$$\delta Q_{\text{mix}} = -Q_{\text{EUC}} \frac{\delta V}{V_f}, \quad (7)$$

where V_f is the final volume of the layer with a $\delta V = V_f - V_{\text{EUC}}$ increment associated with diapycnal mixing. In (7), the transformation of the mean PV of the water column due to diapycnal mixing is proportional to its variation in volume. In our simulations, the total variation of volume for both hemispheres $\delta V \approx -0.25 \text{ Sv}$ is negative, showing that there is a net flux of EUC water into the lower layer because of mixing.

The results for the PV transformation in the EUC are summarized in Figure 7, where we illustrate the processes which modify the EUC PV along its path (Fig. 7a). For particles flowing into the Gulf of Guinea, diapycnal mixing as well as other processes modify the initial Q_{EUC} . During bifurcation, the EUC branches charge across the planetary vorticity gradient, developing local PV anomalies ($Q_a = Q_f - f$; Fig. 7b,c), which are modulated by distinct PV transformation processes. On average, diapycnal mixing attenuates these anomalies, through a net loss of EUC volume to the lower layer. Within the ensemble of other processes, isopycnal mixing generally acts to also buffer the anomalies by mixing local $Q \approx f$ water with the $Q_{\text{EUC}} \approx 0$ water of the EUC bifurcating branches. The local effects of friction on PV depend on the type of friction (bottom or lateral). The effect of bottom friction can, in principle, be predicted and depends on the direction of the current along the topography (D'Asaro, 1988; Benthuisen & Thomas, 2012; Gula et al., 2015, 2016). However, the direction of the instantaneous currents varies so that both positive and negative anomalies are created (see the PV animation in S2). In addition, lateral friction, associated with horizontal viscosity operators, can also play a significant role and its sign cannot be easily predicted (Morel & McWilliams, 2001). Since all these isopycnal processes cannot be quantified in our simulation, we discuss their combined effects in δQ_{other} .

Averaged within our streamtubes, δQ_{mix} and δQ_{other} usually show the same sign, except for the Northern Hemisphere in WI. With the presence of São Tomé, δQ_{other} acts to strengthen the PV anomalies (Fig. 7b,c). In WI, mixing has a stronger impact on the Northern Hemisphere anomalies, accounting for virtually $2/3$ of the PV transformation ($\delta Q_{\text{mix}} = 7.2 \times 10^{-7} \text{ s}^{-1}$ and $\delta Q_{\text{other}} = -3.5 \times 10^{-7} \text{ s}^{-1}$). In the Southern Hemisphere,

735 diapycnal mixing is weaker and the buffering effect due to friction and isopycnal mixing
 736 is stronger. This leads to PV anomalies relative to the background planetary vorticity
 737 that are stronger in the Northern than in the Southern Hemisphere (Fig. 7b). When
 738 the islands are removed, the EUC directly interacts with the continental slope and shelf
 739 waters, with both friction and mixing combined to attenuate the local PV anomalies.
 740 These anomalies in NI are weaker in the Northern Hemisphere than in the Southern Hemisphere,
 741 particularly because δQ_{mix} is larger in the Northern Hemisphere (Fig. 7c). Also,
 742 the anomalies in the Northern Hemisphere of NI are weaker than those in WI, because
 743 δQ_{other} is stronger than, and has opposite sign to, that in WI (compare Fig. 7b and Fig.
 744 7c). The effect of PV transformation on local PV anomalies is thus consistent with the
 745 asymmetry depicted in the mean PV (Fig. 3) and potential enstrophy (Fig. 5) distributions
 746 presented earlier.

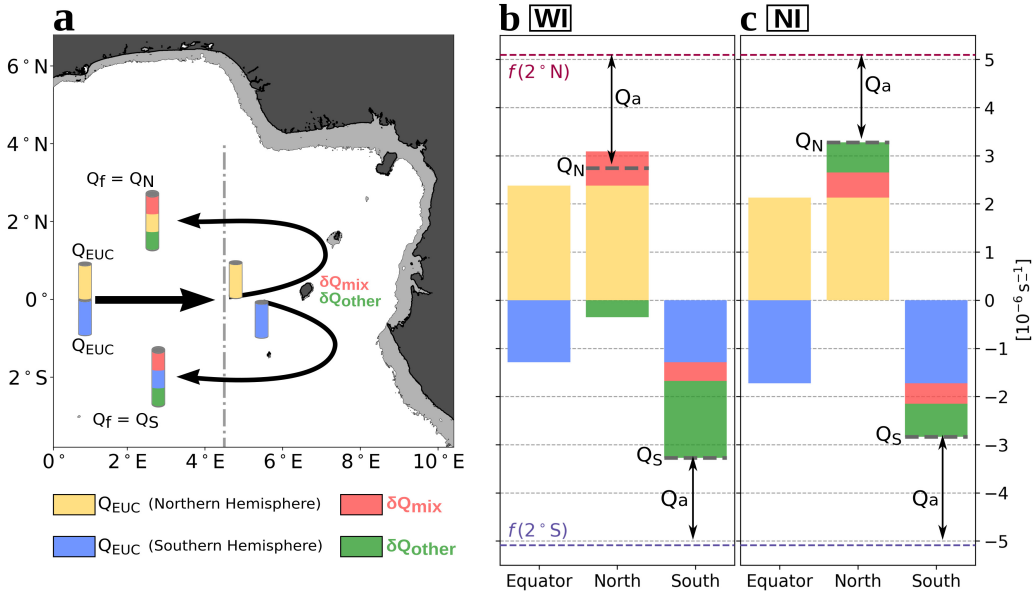


Figure 7. Changes in the EUC PV due to diapycnal mixing and other processes in the Gulf of Guinea. (a) Schematic representation of the problem addressed, where the initial Q_{EUC} at each hemisphere may be transformed by processes within the Gulf of Guinea and return as westward flows. The final Q_f at each hemisphere is the result of this hemisphere’s bulk Q_{EUC} modified by different δQ_{mix} and δQ_{other} . (b) PV transformation in the WI experiment. (c) PV transformation in the NI experiment. Gray dashed lines show Q_f at each hemisphere (Q_N or Q_S ; the sum of the bars). Q_{EUC} : initial bulk PV of the EUC at 4.5° E for each hemisphere; Q_N : PV across the northern transect at 4.5° E ; Q_S : PV across the southern transect at 4.5° E ; δQ_{mix} : PV transformation due to mixing; δQ_{other} : PV transformation due to friction and isopycnal mixing; Q_a : strength of the PV anomaly with respect to the background planetary vorticity.

747 Transformation of PV is key in setting the dynamics of the EUC in the Gulf of Guinea.
 748 Due to the presence of the islands and topography, both friction and diapycnal mixing
 749 must play a prominent role, since flow-topography interactions are known to induce strong
 750 mixing (e.g., Lueck & Mudge, 1997; Naveira Garabato et al., 2004) and introduce PV
 751 anomalies (e.g., Wenegrat et al., 2018; Gula et al., 2019; Napolitano et al., 2021). Assene
 752 et al. (2020) showed that isopycnal mixing also takes place during the rearranging of PV
 753 anomalies into eddies. Those diabatic processes, as well as diapycnal mixing, are gen-

754 erally parameterized in numerical models. Therefore, without rigorous quantitative bud-
755 gets, the complete isolation of each process and where they occur could not be done in
756 the simplified framework presented here. In this matter, the role of the islands (so as the
757 difference between WI and NI) remains an open question due to their proximity with
758 other sources of mixing and friction within the peculiar configuration of the Gulf of Guinea.
759 Future studies are needed on this subject to quantify different processes and improve fu-
760 ture numerical model parameterizations.

761 In our model, diapycnal mixing between adjacent layers points to an erosion of the
762 salinity maximum (i.e., freshening) of the EUC, which can influence the local dynam-
763 ics and the net transport of salt across the tropical Atlantic, motivating us to look closer
764 at the EUC-island regional interaction. Due to high stratification between the EUC and
765 the near-surface waters, we assume that the net diapycnal flux leaving the EUC ($\delta V <$
766 0) is primarily associated with mixing with the lower layer (defined between the 1026.4
767 and 1026.8 kg m^{-3} isopycnals). To understand how mixing occurs around the islands,
768 we turn to salinity diagnostics in the lower layer of the EUC and diagnostics from a re-
769 gional Lagrangian experiment.

770 4.2 The salinity imprint in the lower layer

771 In the eastern Gulf of Guinea, the low-PV, high-salinity tongue of the EUC along
772 the Equator also presents a signature in deeper layers (e.g., Assene et al., 2020). This
773 salty signature is strongest in the innermost portions of the gulf, where the EUC inter-
774 acts with the gulf's islands, although the signal is also traceable within the westward-
775 propagating mesoscale eddies (for details, see Fig. 7d from Assene et al., 2020). In the
776 near-surface layer, exchanges with the EUC are also expected (e.g. Da-Allada et al., 2017),
777 but the EUC imprint in this layer is not as clear as it is in the lower layer (Fig. 8) due
778 to the upper layer dynamics. Thus, the following discussion focuses on the vertical ex-
779 changes between the EUC layer and the lower layer.

780 To qualitatively investigate the imbalance in the salt content depicted by $\lambda < 1$
781 (4) in the last section, we analyze the salinity distribution in the lower layer (defined in
782 Section 4.1). Figure 8a shows the salinity vertically averaged within the lower layer in
783 the WI simulation. We depict a weak eastward flow (using the same velocity scales as
784 Fig. 2), which represents the deeper end of the EUC and practically disappears east of
785 5°E . The salt signature from the EUC is faint along the flow, but drastically increases
786 east of 5°E , forming a salty pool of $S > 35.6$ that stands out upstream of São Tomé.
787 This relatively high-salinity area appears where the EUC is topographically forced to bi-
788 furcate. This suggests that vertical exchanges between the layers occur upstream of and
789 around the islands, where mixing tends to be greatly enhanced (Lueck & Mudge, 1997;
790 Naveira Garabato et al., 2004; Nikurashin & Ferrari, 2010; Whalen et al., 2020), entrain-
791 ing lower-layer fresher waters into the EUC and maximum salinity waters from the EUC
792 into the lower layer. Downstream of the island, other local maxima also appear (with
793 salinity values slightly lower than the salty pool, e.g., at 7°E), possibly associated with
794 a secondary diapycnal mixing region and isopycnal mixing between the salty pool and
795 local waters due to mesoscale activity.

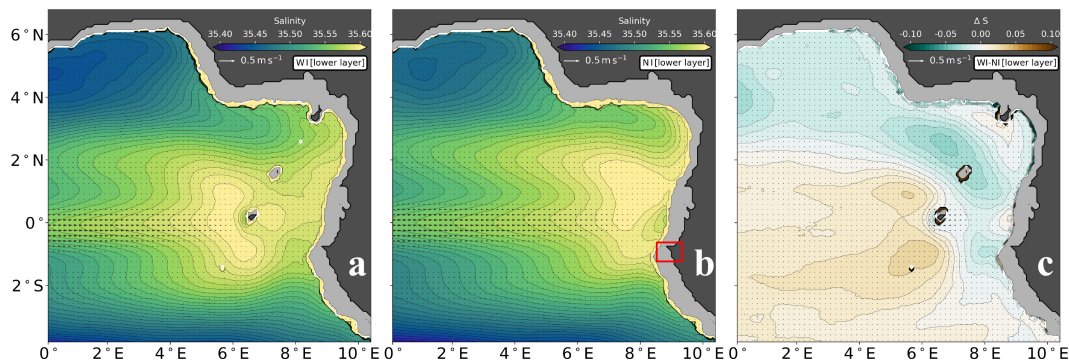


Figure 8. Mean NEMO salinity below the EUC, vertically averaged within the lower layer ($1026.4 - 1026.8 \text{ kg m}^{-3}$) for (a) the NEMO WI simulation, (b) the NEMO NI simulation, where the red rectangle highlights Cape Lopez (Gabon; 1°S , 8.5°E), and (c) the difference between WI and NI. Arrows represent the mean velocity within the layer.

796 In the lower layer of NI (Fig. 8b), the salty pool associated with mixing between
 797 the EUC and the lower layer also appears where the EUC bifurcates, in this case next
 798 to the continental slope. This is reflected in an overall negative ΔS anomaly in the in-
 799 innermost portions of the gulf also in the lower layer (Fig. 8c; see also Fig. 2c). Contrary to
 800 the EUC layer, in the lower layer the imprint of salinity is clearly asymmetric toward
 801 the Northern Hemisphere in NI, probably due to a prominent deeper extension of Cape
 802 Lopez (Gabon; 1°S , 8.5°E ; Fig. 8b) that might restrain the flow. The imprint associ-
 803 ated with the early bifurcation due to São Tomé in Figure 8a is also depicted in Figure
 804 8c by two positive anomalies north and southwest of the island, with a stronger positive
 805 anomaly extending from São Tomé westward along the south corridor, possibly due to
 806 the combination of island-induced mixing in WI and the southern branch partially blocked
 807 at Cape Lopez in NI.

808 To further investigate the changes in salinity derived from the interaction of the
 809 EUC with the Gulf of Guinea islands, we turn at last to a regional Lagrangian study case,
 810 focused on the fate of EUC waters around the islands.

811 4.3 The EUC clash with São Tomé

812 To obtain a detailed view of the EUC bifurcation and tracer modification in the
 813 vicinity of São Tomé Island, we performed a particle tracking experiment with outputs
 814 of the WI simulation. We advected virtual drifters using Parcels v.2.2 framework ([oceanparcels](https://oceanparcels.org)
 815 [.org](https://oceanparcels.org); Delandmeter & Sebille, 2019). Parcels provides a community based, adaptive, and
 816 computationally efficient Lagrangian simulator (cf., Lange & Sebille, 2017; Delandmeter
 817 & Sebille, 2019), extensively used for the computation of ocean particle trajectories
 818 (e.g., Van Sebille et al. (2021); access oceanparcels.org/#peerreviewedarticles for
 819 other examples).

820 In the Gulf of Guinea, we seeded particles within the EUC core layer, dispensed
 821 evenly in a blob spanning $0.5^\circ\text{S} - 0.5^\circ\text{N}$ and $3 - 3.8^\circ\text{E}$. The blob was limited by EUC thresh-
 822 olds of salinity (≥ 35.9), velocity ($\geq 0.5 \text{ m s}^{-1}$), and PV ($|Q| \leq 0.4 \times 10^{-5} \text{ s}^{-1}$), with par-
 823 ticle density increased until reaching an approximately common solution. The 864 par-
 824 ticles released on 20 Sep 2007—before the strong eddy activity observed in Figure 6b—
 825 were advected by the model flow during 40 days, recording latitude, longitude, depth,
 826 and salinity along their trajectories. We time-stepped an evolution equation for $X(t)$,
 827 where X is the three-dimensional position of the particle at time t with a time-step $\delta t =$
 828 5 min , using a 4th order Runge-Kutta integration scheme, which includes vertical veloc-

829 ity. To obtain the salinity diagnostics, we added the salinity fields to the Parcels JIT (just-
 830 in-time) particle class, which already samples the 4D position of the particles (e.g., Lange
 831 & Seville, 2017). Finally, we also added two extra kernel functions, one that deletes par-
 832 ticles that go out of bounds and other to sample salinity values along the float trajec-
 833 tories (see Lange & Seville, 2017, for the detailed definition of the kernels).

834 Different views of the simulated trajectories are displayed in Figure 9. Figure 9a
 835 shows a vertical section of salinity at 3°E (day 1), where the EUC isopycnals 1025.3 and
 836 1026.4 kg m⁻³ delimits the high-salinity band of SMW and SACW. Particles released within
 837 the EUC traveled more than 300 km in about 7 days until reaching the vicinity of São
 838 Tomé. Moments before the impact (day 7), a snapshot of the trajectories captures the
 839 particles flowing with the EUC alongside the Equator from the deployment site at 3°E
 840 to immediately upstream of São Tomé Island at 6°E (Fig. 9a). On the following days,
 841 the trajectories bifurcate while the EUC negotiates the island’s topography. On day 30,
 842 an aerial west-to-east view (Fig. 9b) displays the bifurcation and its associated mesoscale
 843 activity, particularly an anticyclonic meander in the Northern Hemisphere, developing
 844 in the lee of São Tomé, between this island and Príncipe Island. Figure 9b also captures
 845 the latitudinal spread downstream of the islands, as well as a few trajectories that veer
 846 to the west in both hemispheres, with salinity values lower than the initial values at the
 847 EUC. (Note that we have excluded trajectories with salinity changes greater than 1.5
 848 due to interpolation errors too close to topography.) Finally, on the last day of the ex-
 849 periment, Figure 9c poses a view from below, focusing on particles that headed back west
 850 after interacting with the islands’ topography. Interestingly, trajectories presented great
 851 changes in depth immediately upstream and while negotiating the island, with remark-
 852 able downwelling accompanied by (but not necessarily related to) a salinity decrease in
 853 the trajectories veering westward (Fig. 9c). This intense downwelling upstream of São
 854 Tomé brings the EUC waters into the lower layer. Such downwelling events may also con-
 855 tribute to the salty pool observed in the lower layer (Figure 8). Also in Figure 9c, we
 856 depict upwelling particles that also freshen while navigating near São Tomé.

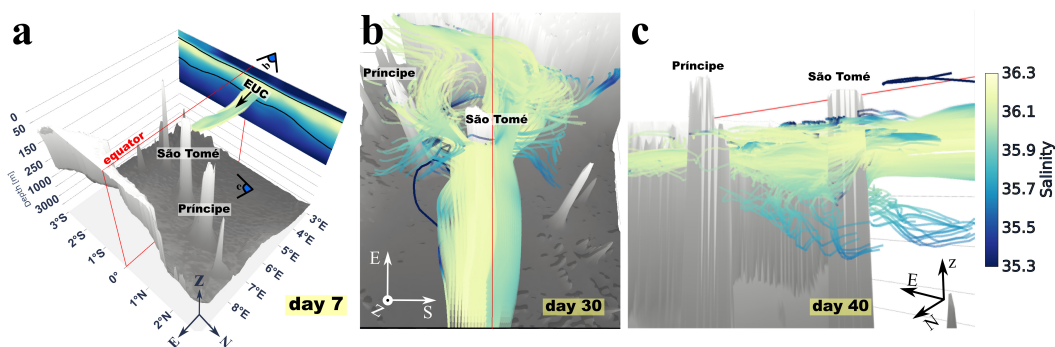


Figure 9. Snapshots from different angles for the trajectories in the Lagrangian simulation. Colors represent salinity, and lines represent individual trajectories from virtual floats deployed within the EUC limits at 3°E, and then advected for 40 days. (a) 3D view (perspective from the African continent) of trajectories at day 7 of the Lagrangian simulation, with the arrow indicating the eastward EUC flow. A vertical section of salinity on day zero shows the EUC layer, delimited by the 1025.3 and 1026.4 kg m⁻³ isopycnals (black lines). The blue semicircles tagged b and c indicate the viewer position for panels b and c, respectively. (b) Trajectories highlighting the mesoscale activity associated with São Tomé and Príncipe Islands on day 30 (aerial view from 0°N, 3°E towards the continent). (c) Trajectories capturing the vertical displacements and salinity changes on day 40 (perspective from the bottom of the ocean at 1°N, 4°E towards the continent).

857 To better understand the fate of floats due to the interaction of the EUC with São
 858 Tomé, we retrieved quantitative diagnostics from the Lagrangian experiment. First, we
 859 defined a time t' relative to the float position with respect to São Tomé Island. When
 860 trajectories approach the island from the west (upstream), $t' = 0$ represents the day
 861 that the float was closest to São Tomé, being at least 10 km from the island and no more
 862 than 100 km away from it. Second, we re-indexed the trajectories by t' and selected the
 863 position at $t' = 30$ for particles that stayed at least within a 120-km-radius from the
 864 island. From the 864 particles deployed initially, 199 (23%) met the criteria above. For
 865 those particles, we observe changes in depth $Z' = Z(t') - Z(t' = -9)$ and salinity $S' =$
 866 $S(t') - S(t' = -9)$ through the probability density function (pdf) of these quantities
 867 binned within their values along trajectories (e.g., Van Sebille et al., 2018) for different
 868 times relative to São Tomé (Fig. 10). In the following discussion, $Z' < 0$ represents sink-
 869 ing and $S' < 0$ represents freshening.

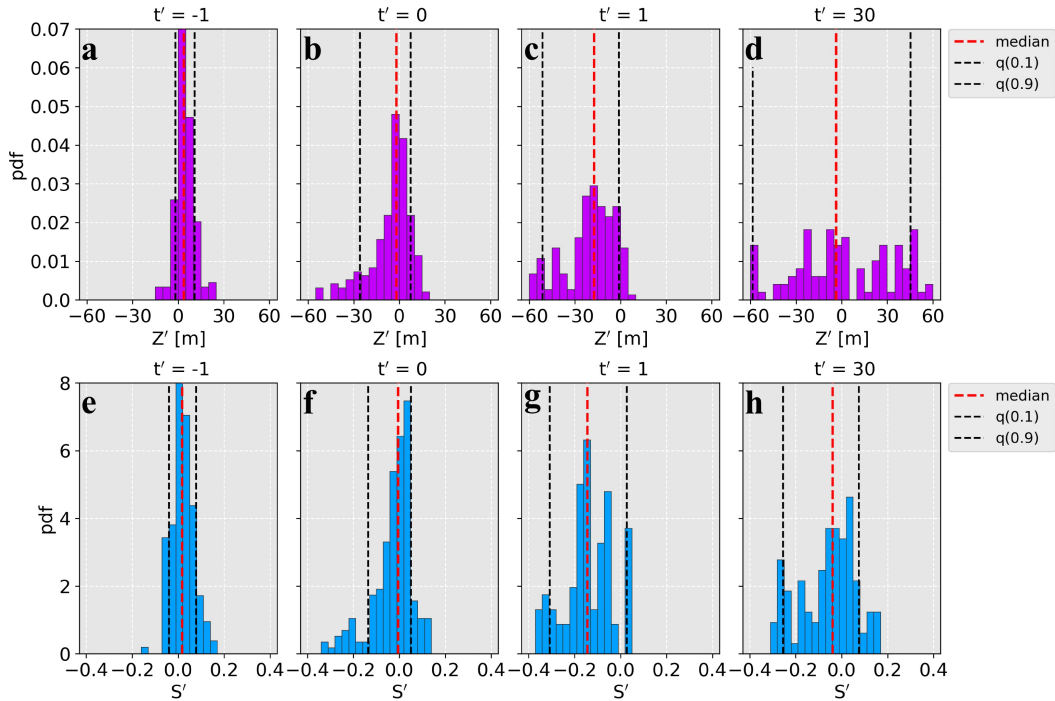


Figure 10. Probability density function for changes in depth and salinity along 40 days of particle trajectory, relative to the EUC encounter with São Tomé at $t' = 0$. (a–d) Pdf of the depth changes (Z') in different times t' relative to São Tomé. (e–h) Pdf of the salinity changes (S') in different times t' relative to São Tomé. Red dashed lines represent the median value of the distribution and black dashed lines represent its 0.1 and 0.9 quantiles. For (a) and (e), the y-axis is limited for better visualization, with maximum pdf values of 0.09 and 11.42 for Z' and S' , respectively. $Z' < 0$ indicates sinking and $S' < 0$ indicates freshening.

870 Particles carried by the EUC approached São Tomé with mean depth and salin-
 871 ity values typical of this eastward flow, 96 ± 19 m and 36.10 ± 0.09 , respectively. In median
 872 values, one day before reaching the island, $\sim 80\%$ of the particles showed only slight
 873 displacements (no more than ± 4 m) and virtually the same salinity ($< \pm 0.05$) from the
 874 EUC depth and salinity at $t' = -9$ (Fig. 10a,e). At the last position upstream of the
 875 island ($t' = 0$), the tail in the pdf and the shift of the 0.1 quantile hints at particles start-
 876 ing to sink and lose salt when approaching São Tomé (Fig. 10b,f). Immediately down-

877 stream of the island, strong downwelling at $t' = 1$ sinks 90% of the particles (Fig. 10c),
 878 with median values of 17 m and 10% of particles sinking > 50 m below Z_0 . As does sink-
 879 ing, freshening also increases from $t'=0$ to $t'=1$, with $\sim 90\%$ of the particles presenting
 880 a negative anomaly and overall S' median values of -0.15 . Further downstream, parti-
 881 cles undergo strong changes in Z' before stabilizing from $t' \sim 10$ (not shown). At the
 882 end of the experiment ($t' = 30$), the Z' distribution has drastically changed, with origi-
 883 nal EUC particles vertically moving $Z' = \pm 60$ m (Fig. 10d). From the S' distribution,
 884 we observe an overall freshening of the EUC after the interaction with São Tomé: if on
 885 the one hand the upper 10% of the distribution (0.9 quantile) has not moved from $t'=-$
 886 1 to $t'=30$ (~ 0.07), on the other hand the lower limit (0.1 quantile) decreased from -0.04
 887 to -0.25 , with a net median decrease of 0.06 (Fig. 10h).

888 The initial EUC-island encounter favours downwelling, also triggering mesoscale
 889 activity and mixing. Downstream of the island, both downwelling and upwelling seems
 890 to occur. While vertical advection is directly associated with changes in Z' , mixing that
 891 changes S' can also affect the particle's depth by generating density anomalies, which
 892 will trigger vertical motions towards equilibrium. Since particles simultaneously sink and
 893 lose salt (Fig. 10b,g; see also Qu et al., 2013), it is probable that mixing with the lower
 894 layer occurs, with the stabilization of trajectories at different depth levels pointing to
 895 density changes. Downwelling and mixing of maximum salinity water also plays a role
 896 in the formation and transport of the Pacific EUC waters, dampening the “source wa-
 897 ters” signal (e.g., Qu et al., 2013) and in the freshening of the Red Sea Overflow Water
 898 in the Arabian Sea (e.g., Menezes, 2021). Using a particle-tracking approach to infer changes
 899 in passive tracers can be sensitive to time sampling and spatial interpolation. Therefore,
 900 we encourage future sensitivity studies addressing the role of particle-tracking numeri-
 901 cal schemes in the potential non-conservation of passive tracers in the absence of mix-
 902 ing.

903 Although comprising a particular event over 40 days, our Lagrangian study case
 904 can be considered representative of the model dynamics near the islands within the EUC
 905 layer, i.e., the vertical motions highlighted in Figures 9c and discussed above are also rep-
 906 resented in the model vertical velocity w (Fig. 11). In Figure 11, we first calculate the
 907 divergence field of the EUC-layer horizontal velocities, $\nabla_{\text{H}} \cdot \mathbf{u} = \partial_x u + \partial_y v$, then ob-
 908 taining w within regions of strong convergence and divergence. (For the mean divergence
 909 curves displayed in Fig. 11a, we used the time-mean horizontal velocity.) The EUC-layer
 910 mean vertical velocity w shows the greatest values ($\pm 6 \times 10^{-6} \text{ m s}^{-1}$) near São Tomé
 911 (Fig. 11a). West (upstream) of the island, a large downwelling region with negative verti-
 912 cal velocity appears, associated with strongest *mean* convergence ($-1 \times 10^{-6} \text{ s}^{-1}$) where
 913 the EUC decelerates approaching São Tomé. Downstream, positive mean velocity domi-
 914 nates, particularly on the sides of the island, where a divergence zone is created between
 915 the EUC branches flowing north and southward and the EUC (Fig. 11a). In glider sec-
 916 tions around the Galápagos, Jakoboski et al. (2020) reported weak vertical velocities at
 917 the Pacific EUC layer. But in the Galápagos case, a vertical spread in the bifurcating
 918 branches compensates for convergence when the EUC approaches the island, resulting
 919 in (integrated) upwelling (Jakoboski et al., 2020).

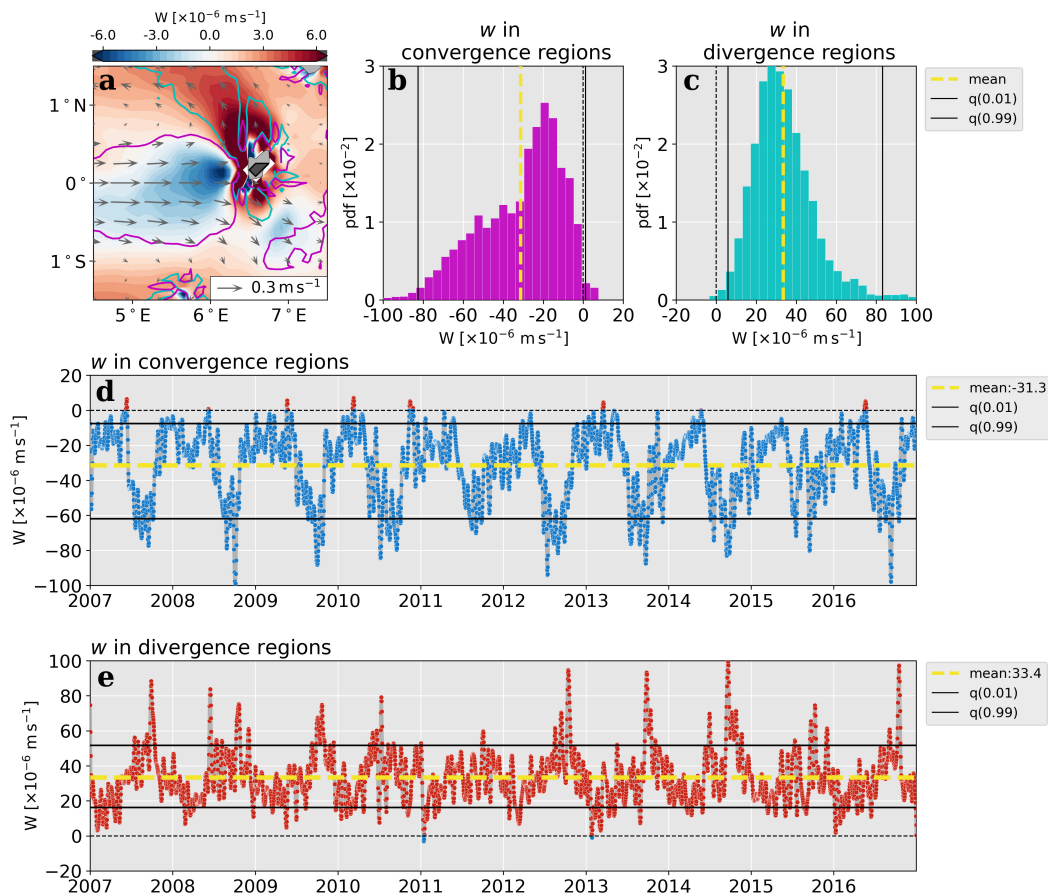


Figure 11. NEMO vertical velocity vertically averaged within the EUC layer. (a) Time-mean horizontal distribution of the vertical velocity (colors), with arrows representing the layer’s mean horizontal velocity; the magenta and cyan curves are obtained from the time-mean horizontal velocity as $\partial_x \bar{u} + \partial_y \bar{v}$ and delimit (with values $\pm 10^{-6} \text{ s}^{-1}$) the mean convergence and divergence regions around São Tomé Island, respectively. In (b–e), vertical velocities are obtained within daily strong convergence/divergence contours (i.e., below and above the 0.05 and 0.95 quantiles of the divergence field distribution, respectively), displayed as: (b,c) pdf of the 7-day-filtered model vertical velocities within the convergence and divergence regions. (d,e) time series of the 7-day-filtered model vertical velocities within the convergence and divergence regions. Positive values (red) indicate upward vertical velocities, while negative values (blue) indicate downward vertical velocities.

920 Time-averaging w in the domain, and remembering that the EUC undergoes seasonal
 921 and higher-frequency variability when interacting with the islands, fluctuations of
 922 the vertical velocity yielded standard deviations much greater than the mean for Fig-
 923 ure 11a. To get a clearer picture of the dynamics due to the EUC interaction with São
 924 Tomé, we evaluate w within curves of strong convergence and divergence (i.e., below
 925 and above the 0.05 and 0.95 quantiles of the divergence field distribution, respectively)
 926 that changed daily within the limits of Figure 11a. While convergence is generally associated
 927 with the EUC approaching the islands, divergence regions are created between the is-
 928 land and the EUC branches that veer northwest and southwestward. Figure 11b-e show
 929 the distribution and time series of the 7-day filtered model vertical velocity, capturing

930 persistent downwelling upstream and upwelling downstream of São Tomé in the latter
 931 half of every year. Within the EUC layer, both upwelling and downwelling occur at each
 932 region, in a “vertical bifurcation” pattern similar to that inferred by Karnauskas et al.
 933 (2010) for the Pacific EUC encounter with the Galápagos. Nevertheless, averaging w within
 934 the EUC layer, downwelling occurs $> 99\%$ of the time in the vertical velocity series within
 935 convergence regions (Fig. 11b,d), with $w = -31.3 \times 10^{-6} \pm 20.5 \times 10^{-6} \text{ m s}^{-1}$. The
 936 downwelling also reflects the seasonal and higher-frequency variability of the EUC, with
 937 strong downwelling opposing eddy-formation periods (compare the peaks between Figs.
 938 11b and 6b). The contrary occurs for divergence regions: on average, upwelling domi-
 939 nates $> 99\%$ of the time series, with similar magnitude ($33.4 \times 10^{-6} \pm 15.0 \times 10^{-6} \text{ m s}^{-1}$)
 940 and peaks (visually) correlated with strong downwelling periods (Fig. 11c,e).

941 We here remind the reader that this analysis represent diagnostics from a numer-
 942 ical simulation which, like every other model, presents strengths and weaknesses. If on
 943 the one hand the staircase bathymetry of our simulation allows the representation of steep
 944 volcanic islands (which would have been severely smoothed in a sigma-coordinate model
 945 at this resolution), on the other hand this may introduce numerical uncertainties in the
 946 vertical velocity and modeling of the bottom friction compared with sigma-coordinate
 947 models. However, by comparing regions next to and far from the islands, we reasoned
 948 that potential numerical w uncertainties introduced by boundary effects would not likely
 949 alter our conclusions.

950 To conclude, we showed that the EUC slowing down upstream of São Tomé cre-
 951 ates convergence regions that cause sustained downwelling. Downstream of the island,
 952 these waters upwell within the EUC layer. Strong vertical velocities modulated by the
 953 EUC seasonal dynamics (Fig. 11) may also have an impact on eddy formation and con-
 954 sequently on the net fluxes between the eastern and western tropical Atlantic. Regions
 955 of strong vertical motions are also generally indicative of mixing, since important changes
 956 in salinity (Fig. 10f) modify the particles’ density, forcing them to readjust to depth lev-
 957 els as a function of an evolving density.

958 5 Final Remarks

959 Observations that capture the EUC upstream of and aligned with São Tomé Island
 960 indicate an inevitable collision between this strong current and the island’s topography.
 961 Using two NEMO simulations that differ only in the presence versus absence of the is-
 962 lands in the Gulf of Guinea, we show that the EUC bifurcates earlier at São Tomé when
 963 the island is present, generating mesoscale activity downstream and mesoscale anticy-
 964 clonic eddies that propagate westward. This encounter is the main driver of subsurface
 965 flow-topography interactions in the Gulf of Guinea, which affect the region’s meso-to-
 966 large scale circulation and fuels the inverse energy cascade.

967 In the meso-to-large-scale circulation, anticyclonic eddies generated at the EUC bi-
 968 furcation carry salinity and PV through zonal corridors into the western tropical Atlantic,
 969 bringing anomalies that drive the large-scale circulation and tracer patterns. The eddy-
 970 formation process involves not only the EUC branches crossing the planetary vorticity
 971 gradient and developing local anticyclonic PV anomalies, but also transformation of PV
 972 through diapycnal mixing and friction and isopycnal mixing, which combined will act
 973 to attenuate the anomalies. Acting as a physical barrier, São Tomé is directly respon-
 974 sible for forcing the EUC bifurcation at $\sim 6.5^\circ\text{E}$, causing a large spread of high-salinity
 975 and low-PV waters downstream of the islands. The islands also prevent the EUC wa-
 976 ters from reaching the innermost portions of the gulf, for instance the region around Bioko
 977 Island. The EUC-São Tomé interactions present a seasonal and interannual variability
 978 that is reflected in an equatorial asymmetry in the strength and formation rate of the
 979 westward-propagating eddies. In a nutshell, a weaker EUC hinders eddy formation dur-
 980 ing seasonal equatorial upwelling whereas a strong EUC boost the number and strength

of eddies formed, with seasonal and interannual meridional displacements northward potentially adding to this increase.

Virtual float trajectories in a regional Lagrangian experiment generally show downwelling as the EUC approaches São Tomé. Downstream of the islands, intense mixing drives salinity changes. At the same time, particles move up and down the water column, stabilizing at new depth levels due to density changes, with a net downwelling and freshening of the EUC waters. The brief experiment is backed up by the model vertical velocities, which show downwelling hotspots associated with convergence of the EUC upstream of São Tomé, followed by downstream strong divergence-upwelling sites on the flanks of the island.

To advance in the understanding of the EUC interaction with the islands of the Gulf of Guinea, several topics addressed in this study demand further attention, for example, the thorough assessment of the spatial and timescales of the EUC variability near its termination site, the mechanisms controlling the generation of PV anomalies, the relation between vertical velocities and eddy formation, and how different models reproduce the dynamics adjacent to the islands. In addition, future work will need to further explore the vertical structure of vertical velocities within the EUC layer and the biogeochemical impacts of flow-topography interactions in the Gulf of Guinea. The EUC transports high oxygen and low nutrient waters, and its interaction with the islands forces upwelling and downwelling, as well as redistribution of these waters by vertical advection and mixing processes through meso- and submesoscale dynamics. All these processes embedded in a background of nutrient-rich coastal water and low-oxygen deeper layers are likely to impact the productivity and oxygen minimum zone in the Gulf of Guinea.

Acknowledgments

We thank Frank O. Smith for copy editing and proofreading this manuscript and three anonymous reviewers for their contribution that improved the manuscript. This study was supported by the TRIATLAS project, which has received funding from the European Union's Horizon 2020 research and innovation program under grant agreement 817578. This study is also supported by the project SWOT-GG, funded by CNES (grant 6009-4500066497). We thank the French PIRATA Observation Service for the deployment of the PIRATA moorings and the ADCP measurements used in this work. We also acknowledge the GTMBA Project Office of NOAA/PMEL for the distribution of the data from the PIRATA moored array. Supercomputing facilities were provided by the GENCI project GEN7298. The French PIRATA cruises and the Enhanced PIRATA dataset are publicly available at <https://www.seanoe.org/data/00335/44635/> and <https://www.pmel.noaa.gov/tao/drupal/disdel/>, respectively. The processed model outputs used in this study can be distributed on demand. Animation within the supplementary information can be obtained at <https://jmp.sh/QOM2NF2>.

References

- Alory, G., Da-Allada, C. Y., Djakouré, S., Dadou, I., Jouanno, J., & Loemba, D. P. (2021). Coastal upwelling limitation by onshore geostrophic flow in the Gulf of Guinea around the Niger River plume. *Frontiers in Marine Science*, 7, 1116. doi: 10.3389/fmars.2020.607216
- Argo. (2020). *Argo float data and metadata from Global Data Assembly Centre (Argo GDAC)*. SEANOE. Retrieved from <https://argo.ucsd.edu> doi: 10.17882/42182#76230
- Arístegui, J., Sangrá, P., Hernández-León, S., Cantón, M., Hernández-Guerra, A., & Kerling, J. L. (1994). Island-induced eddies in the canary islands. *Deep Sea Research Part I: Oceanographic Research Papers*, 41(10), 1509–1525. doi: 10.1016/0967-0637(94)90058-2

- 1031 Assene, F., Morel, Y., Delpéch, A., Aguedjou, M., Jouanno, J., Cravatte, S., ...
 1032 Koch-Larrouy, A. (2020). From mixing to the large scale circulation: How the
 1033 inverse cascade is involved in the formation of the subsurface currents in the
 1034 Gulf of Guinea. *Fluids*, 5(3), 147. doi: 10.3390/fluids5030147
- 1035 Awo, F. M., Alory, G., Da-Allada, C. Y., Delcroix, T., Jouanno, J., Kestenare, E., &
 1036 Baloitcha, E. (2018). Sea surface salinity signature of the Tropical Atlantic in-
 1037 terannual climatic modes. *Journal of Geophysical Research: Oceans*, 123(10),
 1038 7420–7437. doi: 10.1029/2018JC013837
- 1039 Bachelery, M. L., Illig, S., & Dadou, I. (2016). Interannual variability in the South-
 1040 East Atlantic Ocean, focusing on the Benguela Upwelling System: remote
 1041 versus local forcing. *Journal of Geophysical Research: Oceans*, 121(1), 284–
 1042 310. doi: 10.1002/2015JC011168
- 1043 Benthuyssen, J., & Thomas, L. N. (2012). Friction and diapycnal mixing at a slope:
 1044 boundary control of potential vorticity. *Journal of Physical Oceanography*,
 1045 42(9), 1509–1523. doi: 10.1175/JPO-D-11-0130.1
- 1046 Blanke, B., Arhan, M., Lazar, A., & Prévost, G. (2002). A Lagrangian numerical
 1047 investigation of the origins and fates of the salinity maximum water in the
 1048 Atlantic. *Journal of Geophysical Research: Oceans*, 107(C10), 27–1. doi:
 1049 10.1029/2002JC001318
- 1050 Blanke, B., & Delecluse, P. (1993). Variability of the Tropical Atlantic Ocean
 1051 simulated by a general circulation model with two different mixed-layer
 1052 physics. *Journal of Physical Oceanography*, 23(7), 1363–1388. doi:
 1053 10.1175/1520-0485(1993)023<1363:VOTTAO>2.0.CO;2
- 1054 Blayo, E., & Debreu, L. (1999). Adaptive mesh refinement for finite-difference ocean
 1055 models: first experiments. *Journal of Physical Oceanography*, 29(6), 1239 -
 1056 1250. doi: 10.1175/1520-0485(1999)029<1239:AMRFFD>2.0.CO;2
- 1057 Bourlès, B., Araujo, M., McPhaden, M. J., Brandt, P., Foltz, G. R., Lumpkin, R.,
 1058 ... Perez, R. C. (2019). PIRATA: A sustained observing system for Tropi-
 1059 cal Atlantic climate research and forecasting. *Earth and Space Science*, 6(4),
 1060 577–616. doi: 10.1029/2018EA000428
- 1061 Bourlès, B., Herbert, G., Rousselot, P., & Grelet, J. (2018). *French PIRATA cruises:*
 1062 *S-ADCP data*. SEANOE. Retrieved from [https://www.seanoe.org/data/
 1063 00335/44635/](https://www.seanoe.org/data/00335/44635/) doi: 10.17882/44635
- 1064 Bourlès, B., Lumpkin, R., McPhaden, M. J., Hernandez, F., Nobre, P., Campos, E.,
 1065 ... Servain-Jacques, T. J. (2008). The PIRATA program: History, accomplish-
 1066 ments, and future directions. *Bulletin of the American Meteorological Society*,
 1067 89(8), 1111–1126. doi: 10.1175/2008BAMS2462.1
- 1068 Brandt, P., Funk, A., Hormann, V., Dengler, M., Greatbatch, R. J., & Toole, J. M.
 1069 (2011). Interannual atmospheric variability forced by the deep Equatorial
 1070 Atlantic Ocean. *Nature*, 473(7348), 497–500. doi: 10.1038/nature10013
- 1071 Brandt, P., Funk, A., Tantet, A., Johns, W. E., & Fischer, J. (2014). The
 1072 Equatorial Undercurrent in the Central Atlantic and its relation to tropi-
 1073 cal atlantic variability. *Climate Dynamics*, 43(11), 2985–2997. doi:
 1074 10.1007/s00382-014-2061-4
- 1075 Brandt, P., Hahn, J., Schmidtko, S., Tuchen, F. P., Kopte, R., Kiko, R., ... Den-
 1076 gler, M. (2021). Atlantic Equatorial Undercurrent intensification counteracts
 1077 warming-induced deoxygenation. *Nature Geoscience*, 14(5), 278–282. doi:
 1078 10.1038/s41561-021-00716-1
- 1079 Brandt, P., Schott, F. A., Provost, C., Kartavtseff, A., Hormann, V., Bourlès, B., &
 1080 Fischer, J. (2006). Circulation in the central Equatorial Atlantic: mean and
 1081 intraseasonal to seasonal variability. *Geophysical Research Letters*, 33(7). doi:
 1082 10.1029/2005GL025498
- 1083 Bretherton, F. P., & Haidvogel, D. B. (1976). Two-dimensional turbulence
 1084 above topography. *Journal of Fluid Mechanics*, 78(1), 129–154. doi:
 1085 10.1017/S002211207600236X

- 1086 Cane, M. A., & Moore, D. W. (1981). A note on low-frequency equatorial basin
1087 modes. *Journal of Physical Oceanography*, *11*(11), 1578–1584. doi: 10.1175/
1088 1520-0485(1981)011<1578:ANOLFE>2.0.CO;2
- 1089 Chang, P., Zhang, R., Hazeleger, W., Wen, C., Wan, X., Ji, L., . . . Seidel, H. (2008).
1090 Oceanic link between abrupt changes in the North Atlantic Ocean and the
1091 African monsoon. *Nature Geoscience*, *1*(7), 444–448. doi: 10.1038/ngeo218
- 1092 Charney, J. G. (1971). Geostrophic turbulence. *Journal of the Atmospheric Sci-*
1093 *ences*, *28*(6), 1087–1095. doi: 10.1175/1520-0469(1971)028<1087:GT>2.0.CO;2
- 1094 Copernicus Climate Change Service, C. (2017). *ERA5: Fifth generation of ECMWF*
1095 *atmospheric reanalyses of the global climate*. Copernicus Climate Change Ser-
1096 vice Climate Data Store (CDS). Documentation May 2019. Retrieved from
1097 <https://cds.climate.copernicus.eu/cdsapp#!/home>
- 1098 Da-Allada, C. Y., Jouanno, J., Gaillard, F., Kolodziejczyk, N., Maes, C., Reul, N.,
1099 & Bourlès, B. (2017). Importance of the Equatorial Undercurrent on the sea
1100 surface salinity in the eastern Equatorial Atlantic in boreal spring. *Journal of*
1101 *Geophysical Research: Oceans*, *122*(1), 521–538. doi: 10.1002/2016JC012342
- 1102 D’Asaro, E. A. (1988). Generation of submesoscale vortices: a new mechanism.
1103 *Journal of Geophysical Research: Oceans*, *93*(C6), 6685–6693. doi: 10.1029/
1104 JC093iC06p06685
- 1105 Delandmeter, P., & Seville, E. v. (2019). The Parcels v2.0 Lagrangian framework:
1106 new field interpolation schemes. *Geoscientific Model Development*, *12*(8),
1107 3571–3584. doi: 10.5194/gmd-12-3571-2019
- 1108 Delpech, A., Cravatte, S., Marin, F., Morel, Y., Gronchi, E., & Kestenare, E.
1109 (2020). Observed tracer fields structuration by middepth zonal jets in the
1110 Tropical Pacific. *Journal of Physical Oceanography*, *50*(2), 281 - 304. doi:
1111 10.1175/JPO-D-19-0132.1
- 1112 ETOPO2. (2001). *National Geophysical Data Center, NESDIS, NOAA, U.S.*
1113 *Department of Commerce. Global 2 Arc-minute Ocean Depth and Land El-*
1114 *evation from the US National Geophysical Data Center (NGDC)*. Boul-
1115 der CO: Research Data Archive at the National Center for Atmospheric
1116 Research, Computational and Information Systems Laboratory. doi:
1117 <https://doi.org/10.5065/D6668B75>
- 1118 Ferry, N., Parent, L., Garric, G., Bricaud, C., Testut, C. E., Le Galloudec, O., . . .
1119 Zawadzki, L. (2012). GLORYS2V1 global ocean reanalysis of the altimetric
1120 era (1992–2009) at mesoscale. *Mercator Ocean-Quarterly Newsletter*, *44*.
- 1121 Fofonoff, N., & Montgomery, R. (1955). The Equatorial Undercurrent in the light of
1122 the vorticity equation. *Tellus*, *7*(4), 518–521. doi: 10.3402/tellusa.v7i4.8910
- 1123 Foltz, G. R., Brandt, P., Richter, I., Rodriguez-Fonseca, B., Hernandez, F., Dengler,
1124 M., . . . Reul, N. (2019). The Tropical Atlantic Observing System. *Frontiers in*
1125 *Marine Science*, *6*, 206. doi: 10.3389/fmars.2019.00206
- 1126 Foltz, G. R., Grodsky, S. A., Carton, J. A., & McPhaden, M. J. (2004). Seasonal
1127 salt budget of the northwestern tropical Atlantic Ocean along 38 w. *Journal of*
1128 *Geophysical Research: Oceans*, *109*(C3). doi: 10.1029/2003JC002111
- 1129 Foltz, G. R., Schmid, C., & Lumpkin, R. (2018). An Enhanced PIRATA Dataset for
1130 Tropical Atlantic Ocean Atmosphere Research. *Journal of Climate*, *31*(4), 1499
1131 - 1524. doi: 10.1175/JCLI-D-16-0816.1
- 1132 Goes, M., Molinari, R., da Silveira, I., & Wainer, I. (2005). Retroreflections
1133 of the North Brazil Current during February 2002. *Deep Sea Research*
1134 *Part I: Oceanographic Research Papers*, *52*(4), 647–667. doi: 10.1016/
1135 j.dsr.2004.10.010
- 1136 Gouriou, Y., & Reverdin, G. (1992). Isopycnal and diapycnal circulation of the Up-
1137 per Equatorial Atlantic Ocean in 1983–1984. *Journal of Geophysical Research*,
1138 *97*, 3543–3572. doi: 10.1029/91{JC}02935
- 1139 Gula, J., Blacic, T. M., & Todd, R. E. (2019). Submesoscale coherent vortices in the
1140 gulf stream. *Geophys. Res. Lett.*, *46*. doi: 10.1029/2019GL081919

- 1141 Gula, J., Molemaker, M., & McWilliams, J. (2015). Topographic vorticity genera-
 1142 tion, submesoscale instability and vortex street formation in the Gulf Stream.
 1143 *Geophys. Res. Lett.*, *42*, 40544062. doi: 10.1002/2015GL063731
- 1144 Gula, J., Molemaker, M., & McWilliams, J. (2016). Topographic generation of sub-
 1145 mesoscale centrifugal instability and energy dissipation. *Nature Communica-*
 1146 *tions*, *7*, 12811. doi: 10.1038/ncomms12811
- 1147 Haynes, P. H., & McIntyre, M. E. (1987). On the evolution of vorticity and
 1148 potential vorticity in the presence of diabatic heating and frictional or
 1149 other forces. *Journal of Atmospheric Sciences*, *44*(5), 828–841. doi:
 1150 10.1175/1520-0469(1987)044<0828:OTEOVA>2.0.CO;2
- 1151 Hazeleger, W., de Vries, P., & Friocourt, Y. (2003). Sources of the Equatorial
 1152 Undercurrent in the Atlantic in a high-resolution ocean model. *Journal of*
 1153 *Physical Oceanography*, *33*(4), 677–693. doi: 10.1175/1520-0485(2003)33<677:
 1154 SOTEUI>2.0.CO;2
- 1155 Herbert, G., Bourlès, B., Penven, P., & Grelet, J. (2016). New insights on the upper
 1156 layer circulation north of the Gulf of Guinea. *Journal of Geophysical Research:*
 1157 *Oceans*, *121*(9), 6793–6815. doi: 10.1002/2016JC011959
- 1158 Herbert, G., Kermabon, C., Grelet, J., & Bourles, B. (2015). French PIRATA
 1159 cruises S-ADCP data processing (Computer software manual No. 52). Re-
 1160 trieved from <https://archimer.ifremer.fr/doc/00272/38320/36561.pdf>
- 1161 Hormann, V., & Brandt, P. (2009). Upper equatorial atlantic variability during 2002
 1162 and 2005 associated with equatorial kelvin waves. *Journal of Geophysical Re-*
 1163 *search: Oceans*, *114*(C3). doi: 10.1029/2008JC005101
- 1164 Hoskins, B. J., McIntyre, M. E., & Robertson, A. W. (1985). On the use and sig-
 1165 nificance of isentropic potential vorticity maps. *Quarterly Journal of the Royal*
 1166 *Meteorological Society*, *111*(470), 877–946. doi: 10.1002/qj.49711147002
- 1167 Houndegnonto, O., Kolodziejczyk, N., Maes, C., Bourlès, B., Da-Allada, C., & Reul,
 1168 N. (2021). Seasonal variability of freshwater plumes in the Eastern Gulf
 1169 of Guinea as inferred from satellite measurements. *Journal of Geophysical*
 1170 *Research: Oceans*, *126*(5), e2020JC017041. doi: 10.1029/2020JC017041
- 1171 Illig, S., & Bachèlery, M.-L. (2019). Propagation of subseasonal equatorially-forced
 1172 coastal trapped waves down to the Benguela upwelling system. *Scientific re-*
 1173 *ports*, *9*(1), 1–10. doi: 10.1038/s41598-019-41847-1
- 1174 Jakoboski, J., Todd, R. E., Owens, W. B., Karnauskas, K. B., & Rudnick, D. L.
 1175 (2020). Bifurcation and upwelling of the Equatorial Undercurrent west of the
 1176 Galpagos Archipelago. *Journal of Physical Oceanography*, *50*(4), 887–905. doi:
 1177 10.1175/JPO-D-19-0110.1
- 1178 Johns, W. E., Brandt, P., Bourlès, B., Tantet, A., Papapostolou, A., & Houk,
 1179 A. (2014). Zonal structure and seasonal variability of the Atlantic
 1180 Equatorial Undercurrent. *Climate Dynamics*, *43*(11), 3047–3069. doi:
 1181 10.1007/s00382-014-2136-2
- 1182 Johnson, G. C., Sloyan, B. M., Kessler, W. S., & McTaggart, K. E. (2002). Di-
 1183 rect measurements of upper ocean currents and water properties across
 1184 the tropical pacific during the 1990s. *Prog. Oceanog.*, *52*, 31 - 61. doi:
 1185 10.1016/S0079-6611(02)00021-6
- 1186 Jouanno, J., & Capet, X. (2020). Connecting flow–topography interactions, vor-
 1187 ticity balance, baroclinic instability and transport in the Southern Ocean:
 1188 the case of an idealized storm track. *Ocean Science*, *16*(5), 1207–1223. doi:
 1189 10.5194/os-16-1207-2020
- 1190 Jouanno, J., Marin, F., du Penhoat, Y., & Molines, J.-M. (2013). Intraseasonal
 1191 modulation of the surface cooling in the Gulf of Guinea. *Journal of Physical*
 1192 *Oceanography*, *43*(2), 382–401. doi: 10.1175/JPO-D-12-053.1
- 1193 Jouanno, J., Marin, F., Du Penhoat, Y., Molines, J.-M., & Sheinbaum, J. (2011).
 1194 Seasonal modes of surface cooling in the Gulf of Guinea. *Journal of Physical*
 1195 *Oceanography*, *41*(7), 1408 - 1416. doi: 10.1175/JPO-D-11-031.1

- 1196 Jouanno, J., Marin, F., Du Penhoat, Y., Sheinbaum, J., & Molines, J.-M.
 1197 (2011). Seasonal heat balance in the upper 100 m of the Equatorial At-
 1198 lantic Ocean. *Journal of Geophysical Research: Oceans*, 116(C9). doi:
 1199 10.1029/2010JC006912
- 1200 Karnauskas, K. B., Murtugudde, R., & Busalacchi, A. J. (2007). The effect of the
 1201 Galpagos Islands on the Equatorial Pacific cold tongue. *Journal of Physical*
 1202 *Oceanography*, 37(5), 1266 - 1281. doi: 10.1175/JPO3048.1
- 1203 Karnauskas, K. B., Murtugudde, R., & Busalacchi, A. J. (2008). The effect of the
 1204 Galápagos Islands on ENSO in forced ocean and hybrid coupled models. *Jour-*
 1205 *nal of Physical Oceanography*, 38(11), 2519–2534. doi: 10.1175/2008JPO3848
 1206 .1
- 1207 Karnauskas, K. B., Murtugudde, R., & Busalacchi, A. J. (2010). Observing the gal-
 1208 pagoseuc interaction: Insights and challenges. *Journal of Physical Oceanogra-*
 1209 *phy*, 40(12), 2768 - 2777. doi: 10.1175/2010JPO4461.1
- 1210 Kolodziejczyk, N., Bourlès, B., Marin, F., Grelet, J., & Chuchla, R. (2009). Seasonal
 1211 variability of the Equatorial Undercurrent at 10 w as inferred from recent in
 1212 situ observations. *Journal of Geophysical Research: Oceans*, 114(C6). doi:
 1213 10.1029/2008JC004976
- 1214 Kolodziejczyk, N., Marin, F., Bourlès, B., Gouriou, Y., & Berger, H. (2014). Sea-
 1215 sonal variability of the Equatorial Undercurrent termination and associated
 1216 salinity maximum in the Gulf of Guinea. *Climate Dynamics*, 43(11), 3025–
 1217 3046. doi: 10.1007/s00382-014-2107-7
- 1218 Lange, M., & Seville, E. v. (2017). Parcels v0.9: prototyping a Lagrangian ocean
 1219 analysis framework for the petascale age. *Geoscientific Model Development*,
 1220 10(11), 4175–4186. doi: 10.5194/gmd-10-4175-2017
- 1221 Large, W., & Yeager, S. (2009). The global climatology of an interannually varying
 1222 air-sea flux data set. *Climate dynamics*, 33(2-3), 341–364. doi: 10.1007/s00382
 1223 -008-0441-3
- 1224 Li, Q., Sun, L., & Xu, C. (2018). The lateral eddy viscosity derived from the decay
 1225 of oceanic mesoscale eddies. *Open Journal of Marine Science*, 8(01), 152. doi:
 1226 10.4236/ojms.2018.81008
- 1227 Lueck, R. G., & Mudge, T. D. (1997). Topographically induced mixing around a
 1228 shallow seamount. *Science*, 276(5320), 1831–1833. doi: 10.1126/science.276
 1229 .5320.1831
- 1230 Madec, G., & the NEMO team. (2016). NEMO ocean engine (Computer software
 1231 manual No. 27). Zenodo. doi: 10.5281/zenodo.1464816
- 1232 McCreary, J. P., & Yu, Z. (1992). Equatorial dynamics in a 212-layer model.
 1233 *Progress in Oceanography*, 29(1), 61–132.
- 1234 Mémery, L., Arhan, M., Alvarez-Salgado, X., Messias, M.-J., Mercier, H., Castro,
 1235 C., & Rios, A. (2000). The water masses along the western boundary of the
 1236 South and Equatorial Atlantic. *Progress in Oceanography*, 47(1), 69–98. doi:
 1237 10.1016/S0079-6611(00)00032-X
- 1238 Ménesguen, C., Hua, B. L., Fruman, M. D., & Schopp, R. (2009). Dynamics of the
 1239 combined extra-equatorial and equatorial deep jets in the Atlantic. *Journal of*
 1240 *marine research*, 67(3), 323–346. doi: 10.1357/002224009789954766
- 1241 Menezes, V. V. (2021). Advective pathways and transit times of the red sea overflow
 1242 water in the arabian sea from lagrangian simulations. *Progress in Oceanogra-*
 1243 *phy*, 199, 102697. doi: 10.1016/j.pocean.2021.102697
- 1244 Metcalf, W., Voorhis, A., & Stalcup, M. (1962). The Atlantic equatorial under-
 1245 current. *Journal of Geophysical Research*, 67(6), 2499–2508. doi: 10.1029/
 1246 JZ067i006p02499
- 1247 Montes, I., Colas, F., Capet, X., & Schneider, W. (2010). On the pathways of the
 1248 equatorial subsurface currents in the eastern equatorial pacific and their con-
 1249 tributions to the peru-chile undercurrent. *Journal of Geophysical Research:*
 1250 *Oceans*, 115(C9). doi: 10.1029/2009JC005710

- 1251 Morel, Y., Gula, J., & Ponte, A. (2019). Potential vorticity diagnostics based on
1252 balances between volume integral and boundary conditions. *Ocean Modelling*,
1253 *138*, 23–35. doi: 10.1016/j.ocemod.2019.04.004
- 1254 Morel, Y., & McWilliams, J. (2001). Effects of isopycnal and diapycnal mixing
1255 on the stability of oceanic currents. *Journal of Physical Oceanography*, *31*(8),
1256 2280–2296. doi: 10.1175/1520-0485(2001)031<2280:EOIADM>2.0.CO;2
- 1257 Müller, P. (2006). *The equations of oceanic motions*. Cambridge University Press.
- 1258 Napolitano, D. C., Silveira, I. C. A., Tandon, A., & Calil, P. H. R. (2021). Subme-
1259 soscale phenomena due to the Brazil Current crossing of the Vitória-Trindade
1260 Ridge. *Journal of Geophysical Research: Oceans*, *126*(1), e2020JC016731. doi:
1261 10.1029/2020JC016731
- 1262 Naveira Garabato, A. C., Polzin, K. L., King, B. A., Heywood, K. J., & Visbeck, M.
1263 (2004). Widespread intense turbulent mixing in the Southern Ocean. *Science*,
1264 *303*(5655), 210–213. doi: 10.1126/science.1090929
- 1265 Nikurashin, M., & Ferrari, R. (2010). Radiation and dissipation of internal waves
1266 generated by geostrophic motions impinging on small-scale topography: Ap-
1267 plication to the Southern Ocean. *Journal of Physical Oceanography*, *40*(9),
1268 2025–2042. doi: 10.1175/2010JPO4315.1
- 1269 Pedlosky, J. (1987). An inertial theory of the Equatorial Undercurrent. *Journal*
1270 *of Physical Oceanography*, *17*(11), 1978–1985. doi: 10.1175/1520-0485(1987)
1271 017<1978:AITOTE>2.0.CO;2
- 1272 Pedlosky, J., & Spall, M. A. (2015). The interaction of an eastward-flowing current
1273 and an island: Sub- and supercritical flow. *Journal of Physical Oceanography*,
1274 *45*(11), 2806–2819. doi: 10.1175/JPO-D-15-0061.1
- 1275 Picaut, J. (1983). Propagation of the seasonal upwelling in the eastern Equatorial
1276 Atlantic. *Journal of Physical Oceanography*, *13*(1), 18 - 37. doi: 10.1175/1520
1277 -0485(1983)013<0018:POTSUI>2.0.CO;2
- 1278 Polo, I., Lazar, A., Rodriguez-Fonseca, B., & Arnault, S. (2008). Oceanic Kelvin
1279 waves and Tropical Atlantic intraseasonal variability: 1. Kelvin wave char-
1280 acterization. *Journal of Geophysical Research: Oceans*, *113*(C7). doi:
1281 10.1029/2007JC004495
- 1282 Qu, T., Gao, S., & Fine, R. A. (2013). Subduction of South Pacific tropical water
1283 and its equatorward pathways as shown by a simulated passive tracer. *Journal*
1284 *of Physical Oceanography*, *43*(8), 1551–1565. doi: 10.1175/JPO-D-12-0180.1
- 1285 Rabe, B., Schott, F. A., & Khl, A. (2008). Mean circulation and variability of the
1286 tropical atlantic during 19522001 in the gecco assimilation fields. *Journal of*
1287 *Physical Oceanography*, *38*(1), 177 - 192. doi: 10.1175/2007JPO3541.1
- 1288 Rhines, P. B. (1986). Vorticity dynamics of the oceanic general circulation. *Annual*
1289 *review of fluid mechanics*, *18*(1), 433–497. doi: 10.1146/annurev.fl.18.010186
1290 .002245
- 1291 Roemmich, D., & Gilson, J. (2009). The 2004–2008 mean and annual cycle of tem-
1292 perature, salinity, and steric height in the global ocean from the argo program.
1293 *Progress in oceanography*, *82*(2), 81–100.
- 1294 Sangrà, P., Pascual, A., Rodríguez-Santana, Á., Machín, F., Mason, E., McWilliams,
1295 J. C., . . . Auladell, M. (2009). The Canary Eddy Corridor: A major path-
1296 way for long-lived eddies in the subtropical North Atlantic. *Deep Sea Re-*
1297 *search Part I: Oceanographic Research Papers*, *56*(12), 2100–2114. doi:
1298 10.1016/j.dsr.2009.08.008
- 1299 Schott, F. A., Fischer, J., & Stramma, L. (1998). Transports and pathways of the
1300 upper-layer circulation in the western tropical Atlantic. *Journal of Physical*
1301 *Oceanography*, *28*(10), 1904–1928. doi: 10.1175/1520-0485(1998)028<1904:
1302 TAPOTU>2.0.CO;2
- 1303 Silveira, I. C., Brown, W. S., & Flierl, G. R. (2000). Dynamics of the North Brazil
1304 Current retroflection region from the Western Tropical Atlantic Experiment
1305 observations. *Journal of Geophysical Research: Oceans*, *105*(C12), 28,559–

- 1306 28,583. doi: 10.1029/2000JC900129
- 1307 Snowden, D. P., & Molinari, R. L. (2003). Subtropical cells in the Atlantic Ocean:
1308 an observational summary. In *Elsevier oceanography series* (Vol. 68, pp. 287–
1309 312). Elsevier.
- 1310 Stramma, L., & Schmidtko, S. (2021). Tropical deoxygenation sites revisited to in-
1311 vestigate oxygen and nutrient trends. *Ocean Science*, *17*(3), 833–847. doi: 10
1312 .5194/os-17-833-2021
- 1313 Stramma, L., & Schott, F. (1999). The mean flow field of the Tropical Atlantic
1314 Ocean. *Deep Sea Research Part II: Topical Studies in Oceanography*, *46*(1-2),
1315 279–303. doi: 10.1016/S0967-0645(98)00109-X
- 1316 Tchamabi, C. C., Araujo, M., Silva, M., & Bourlès, B. (2017). A study of the
1317 Brazilian Fernando de Noronha Island and Rocas Atoll wakes in the Tropical
1318 Atlantic. *Ocean Modelling*, *111*, 9–18. doi: 10.1016/j.ocemod.2016.12.009
- 1319 Thomas, L. N. (2005). Destruction of potential vorticity by winds. *J. Phys.*
1320 *Oceanogr.*, *35*(12), 2457–2466. doi: 10.1175/JPO2830.1
- 1321 Van Sebille, E., Griffies, S. M., Abernathy, R., Adams, T. P., Berloff, P., Biastoch,
1322 A., . . . Zika, J. D. (2018). Lagrangian ocean analysis: Fundamentals and
1323 practices. *Ocean Modelling*, *121*, 49–75. doi: 10.1016/j.ocemod.2017.11.008
- 1324 Van Sebille, E., Zettler, E., Wienders, N., Amaral-Zettler, L., Elipot, S., & Lumpkin,
1325 R. (2021). Dispersion of surface drifters in the Tropical Atlantic. *Frontiers in*
1326 *Marine Science*, *7*, 1243. doi: 10.3389/fmars.2020.607426
- 1327 Wenegrat, J. O., Thomas, L. N., Gula, J., & McWilliams, J. C. (2018). Effects
1328 of the submesoscale on the potential vorticity budget of ocean mode waters.
1329 *Journal of Physical Oceanography*, *48*(9), 2141–2165.
- 1330 Whalen, C. B., de Lavergne, C., Garabato, A. C. N., Klymak, J. M., MacKinnon,
1331 J. A., & Sheen, K. L. (2020). Internal wave-driven mixing: governing processes
1332 and consequences for climate. *Nature Reviews Earth & Environment*, 1–16.
1333 doi: 10.1038/s43017-020-0097-z